Check for updates

Received: 21 November 2023 | Revised: 25 January 2024 | Accepted: 17 February 2024

DOI: 10.1002/suco.202301020

ARTICLE

fib CEB-FIP WILEY

Capacity assessment of uncorroded and corroded dapped-end beams by NLFE and strut-and-tie based methods

Beatrice Belletti | **Biagio Calcavecchia** | **Daniele Ferretti** | **Simone Ravasini**

Department of Engineering and Architecture, University of Parma, Parma, Italy

Correspondence
Beatrice Belletti, Department of Engineering and Architecture, University of Parma, Parco Area delle Scienze 181/A, 43124 Parma, Italy.
Email: beatrice.belletti@unipr.it

[Correction added on 26 March, after first online publication: Author names for the second, third and fourth author is updated in this version.]

Abstract

The verification of dapped-end beams degraded by corrosion is a problem, especially for existing bridges in service. This paper proposes a nonlinear finite element (NLFE) modeling procedure and a simple strut-and-tie based procedure for predicting the response of dapped-end beams subjected to chloride corrosion. Firstly, the finite element modeling strategy, based on the adoption of multilayer shell elements and the PARC_CL 2.1 crack model is described. Then, the degradation effects on concrete, rebars, and steel-to-concrete interaction are defined as a function of the propagation period of corrosion. In particular, the effects of corrosion on the reinforcement are modeled by applying a reduction of tensile strength that considers for both the reduction of cross-section and the ultimate strain caused by pitting. Concrete splitting cracking due to volume expansion during rust formation is modeled by reducing the mechanical properties of concrete. Corrosion effects in steel-to-concrete interaction are modeled by applying a bond strength decay to the spring elements connecting corroded rebars—modeled with truss elements—and concrete multilayer shell elements. The proposed finite element procedure is used to study two scenarios based on different spatial distributions of corrosion-prone areas. Subsequently, a simplified analytical approach based on the strut-and-corroded tie method—called S&CT method—is proposed and compared with the finite element outcomes. Finally, the validations of the two proposed methods are presented with respect to a corroded dapped-end beam, showing that corrosion of rebars affects the resistance mechanisms of the dapped-end beam, by reducing both resistance and ductility. The proposed simplified analytical S&CT method provides conservative and safe results compared to the numerical NLFE model and to experimental data.

KEYWORDS

corrosion, dapped-end beams, nonlinear finite element, PARC_CL2.1, reinforced concrete, strut-and-tie model

 © 2024 *fib*. International Federation for Structural Concrete

1 | INTRODUCTION

Dapped-ends are quite common in reinforced concrete structures: for example, at the ends of precast beams or in bridge girders. In recent years, the use of dapped-ends in bridges has been abandoned in many countries due to two main problems: (i) corrosion caused by the ingress of water contaminated with chlorides from de-icing salts, (ii) difficulty of inspection and repair, especially if they are located along the span of the bridge. For these reasons, the problem of verifying the bearing capacity of dapped-end beams in existing bridges is an open one,[1–6] considering also that they are often designed using methods that are now outdated. A review of the methods used in the past to design dapped-ends can be found in Shakir.[7] Among these methods, the most popular were the "stitching rule" (i.e., by assuming a generic inclined crack that detaches a portion of the dapped-end and by writing the equilibrium of the forces on this portion, assuming that the reinforcements passing through the crack yield[8]), and some basic resistant trusses.[9] As stated by Schlaich et al.,[10] dapped-ends have been recognized as D-type zones and they have to be designed according to strut-and-tie (S&T) models, as proposed by standards.[11–13] Different standards, although updated over time, provide different S&T models and reinforcement layouts.

Therefore, the reinforcement placed in the old existing structures often does not correspond to that designed using the S&T models recommended by modern standards[11–13] so the resistant truss must be defined on a case-by-case basis. In addition, sometimes in existing structures the reinforcement layout does not correspond to the as-designed requirements. For all these reasons, a wide variety of reinforcement layouts can be observed in dapped-ends of existing structures, which generally have a detrimental effect on the safety assessment. Indeed, it has been experimentally observed that the reinforcement layout influences the behavior of the dapped-ends both at service and at failure.[14]

Based on the hypothesis of perfectly plastic behavior of resisting trusses, S&T models may be inadequate in the case of anchorage failure or premature rupture of the reinforcements. As these circumstances may be triggered by corrosive phenomena, the use of S&T models for corroded dapped-ends must be carefully considered. Indeed, chloride corrosion induces pitting of the reinforcement, which reduces its ductility[15] and can, in principle, invalidate the assumption of perfectly plastic behavior of the ties. In addition, insufficient anchorage resistance of longitudinal bars, due to corrosion or improper detailing, can lead to brittle failure, again invalidating the assumptions of the S&T method.[16,17]

In all these cases, the nonlinear finite element (NLFE) method becomes a suitable approach to study the behavior of corroded dapped-ends at both the serviceability and ultimate limit states. Several approaches—based on NLFE models—are available in the scientific literature for predicting the response of dapped-ends. In general, the proposed NLFE models are used to perform parametric studies after validation with experimental tests. For example, in References 18–20, the dependence of the dapped-end behavior on the geometry of the nib and the concrete strength was investigated, while in References 21–25 the effects of the amount and position of the main reinforcement and the stirrups were analyzed. In the scientific literature NLFE analyses are used to predict the capacity of dapped-ends under monotonic,[26,27] or dynamic loading.[28,29] In References 30–34, NLFE analyses are used to evaluate the capacity of dapped-ends strengthened with steel fiber-reinforced concrete, carbon fiber-reinforced polymers, external carbon fiber wrapping, or steel plates.

More recently, some NLFE results of degraded dapped-end beams have been presented.[35–41] In particular, Santarsiero et al.[35] proposed a 3D NLFE model for a dapped-end with variable thickness where nonlinear truss elements were embedded in concrete. Reinforcement corrosion effects were simulated by reducing only the transversal cross-section of corroded rebars due to chloride ingress over time to predict the residual ultimate capacity. Chijiwa et al.[36] proposed a 3D NLFE model with different corrosion scenarios affecting the reinforcement. Also in this study, the reinforcement was embedded in concrete and the authors also considered the expansion and cracking induced by corrosion products. Rosso et al.[37] proposed a 3D NLFE model with beam elements to model the reinforcing bars; corrosion was considered as a function of the mass loss, which was used as an input parameter to reduce both the cross-sectional area and the ductility of the rebars. Abeysinghe and Yapa[38] proposed a 2D NLFE model in which the effect of corrosion was modeled by reducing the cross-sectional area of corroded rebars. In References 39–41, 2D and 3D NLFE models and S&T models are used to assess the load-bearing capacity of Gerber saddles in existing bridges, again considering the effects of corrosion by reducing only the cross-section of the corroded rebar, the concrete strength, and the prestressing force, while the reduction of the bond strength was modeled by reducing the yield strength of rebars.

In the above-mentioned works, the NLFE models were validated with respect to experimental test on uncorroded specimens and then they were used to investigate the effects of corrosion on the structural response through

17517648, 2024, 2, Downloaded from https://onlinelibrary.wiley.com/doi/10.1002/suco.202301020 by University Degli Studi Di Parma Settore Biblioteche, Wiley Online Library on [15/05/2024]. See the Terms and Conditions (https://onlinelibrary.wiley.com/terms-and-conditions) on Wiley Online Library for rules of use; OA articles are governed by the applicable Creative Commons License

sensitivity analyses at varying levels of corrosion,[35–41] without experimental validation. In general, for all models of corroded dapped-end beams, the problem of their validation is an open issue, both because of the uncertainties of the corrosion parameters to be used as inputs[42] and because of a lack of experimental tests on corroded dapped-end beams. In addition, the analysis of the state-of-the-art in the scientific literature shows the absence of NLFE approaches that comprehensively consider all the effects that can cause the dapped end beam to fail. In fact, the combined modeling of bond-slip behavior between concrete and corroded reinforcement—capable of predicting anchorage failure—together with the modeling of section loss and ultimate strain reduction of corroded steel—capable of predicting the rebar failure even in the elastic stage—has never been considered.

The present work deals with the NLFE modeling of uncorroded and corroded dapped-end beams by using a multi-layered shell elements approach. The modeling approach with shell elements allows to reduce the time and computer memory required for the NLFE analyses and to accurately describe the distribution of the reinforcement along the thickness. The PARC_CL 2.1 crack model is a fixed crack model used to evaluate the nonlinear behavior of reinforced concrete; it is based on smeared modeling of the reinforcement.[43,44] The model has been previously adopted for the response prediction of several corroded members such as columns subjected to cyclic loading,[45] prestressed beams subjected to three-point bending,[46] panels,[44] core walls in seismic resisting systems,[47] and others.

One of the novelties of this paper is the combined modeling of the main effects induced by pitting corrosion and the validation of the model with a very recent experimental test on a corroded dapped-end beam. The effects of corrosion are considered in terms of the reduction of both the cross-section area and the ultimate strain of corroded rebars and the reduction of the mechanical properties of cracked concrete due to volume expansion caused by rust formation. In addition, for corroded rebars, a discrete modeling of the reinforcement has been adopted to explicitly consider the degraded bond-slip behavior that causes anchorage failure. For this purpose, the reinforcing bars are modeled with truss elements, while nonlinear spring elements are inserted to connect the steel truss elements and the concrete multi-layer elements.

Starting from the outcomes of NLFE model, a novel analytical approach based on the S&T method—called strut-and-corroded tie (S&CT) method—is proposed to easily evaluate the load-bearing capacity of corroded dapped-ends. The S&CT method uses the stress–strain relationship of the most corroded reinforcement—typically the stirrups, which have the lower values of both diameter and concrete cover—to all reinforcements—characterized by higher values of diameter, residual area, and ultimate strain. The proposed methods are applied to some of the most recent experimental tests in the literature. The first case study (Section 2), refers to the experimental test of an uncorroded dapped-end beam tested by Flores Ferreira et al.[48] For this case, after the validation of the model for the uncorroded case, two different corrosion scenarios are applied (Section 3). The corrosion scenarios are characterized by (i) localized corrosion in a region of the dapped-end beam more prone to water stagnation and (ii) global corrosion in the external faces of the dapped-end beam. In the second case study (Section 4), the models are validated by comparing the NLFEA and the S&CT method with the result of the recent experimental test on an artificially-corroded dapped-end beam performed by Di Carlo et al.[49] As previously stated, there is a lack of scientific literature that validates NLFEA response predictions with experimental test results. This paper presents the innovative validation of the proposed NLFEA procedure and the S&CT method by comparing them with experimental outcomes from tests on corroded dapped-end beams, which have detailed measurements of the reduced cross-sections of corroded bars.

2 | CASE STUDY 1: DEVELOPMENT AND VALIDATION OF MODELING STRATEGY FOR UNCORRODED DAPPED-END BEAMS

2.1 | Geometry, instrumentation layout, and mechanical properties of concrete and reinforcing steel

The uncorroded dapped-end beam described in Flores Ferreira et al.[48] was selected as a first reference case study for the validation of the proposed modeling strategy. The validation of the approach in the case of corroded dapped-end beams will be presented in Section 4 for the second case study.[50]

The geometry and the boundary conditions of the experimental setup of the dapped-end beam are shown in Figure 1. The thickness of the beam is equal to 250 mm and steel plates are used to apply the vertical load (1) and as supports (2 and 3). The reinforcement layout of the dapped-end beam is designed according to the S&T models proposed in Eurocode 2,[11] and is shown in Figure 2. To ensure anchorage, bars and stirrups are welded on each other. At the intrados of the nib, only the horizontal parts of U-shaped bars have straight anchorages (Figure 2). Since the slip of these straight horizontal

17517648, 2024, 2, Downloaded from https://onlinelibrary.wiley.com/doi/10.1002/suco.202301020 by University Degli Studi Di Parma Settore Biblioteche, Wiley Online Library on [15/05/2024]. See the Terms and Conditions (https://onlinelibrary.wiley.com/terms-and-conditions) on Wiley Online Library for rules of use; OA articles are governed by the applicable Creative Commons License

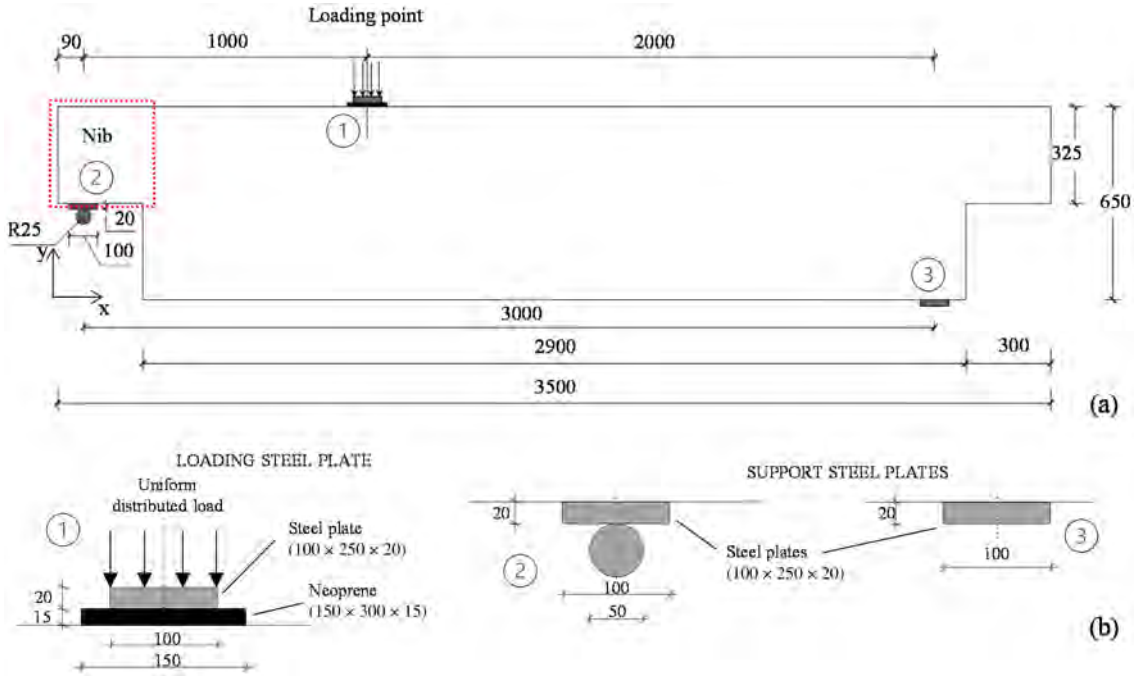

FIGURE 1 Geometry of the dapped-end beam (a) and steel plates (b). Dimensions in mm. *Source:* Adapted from Reference 48.

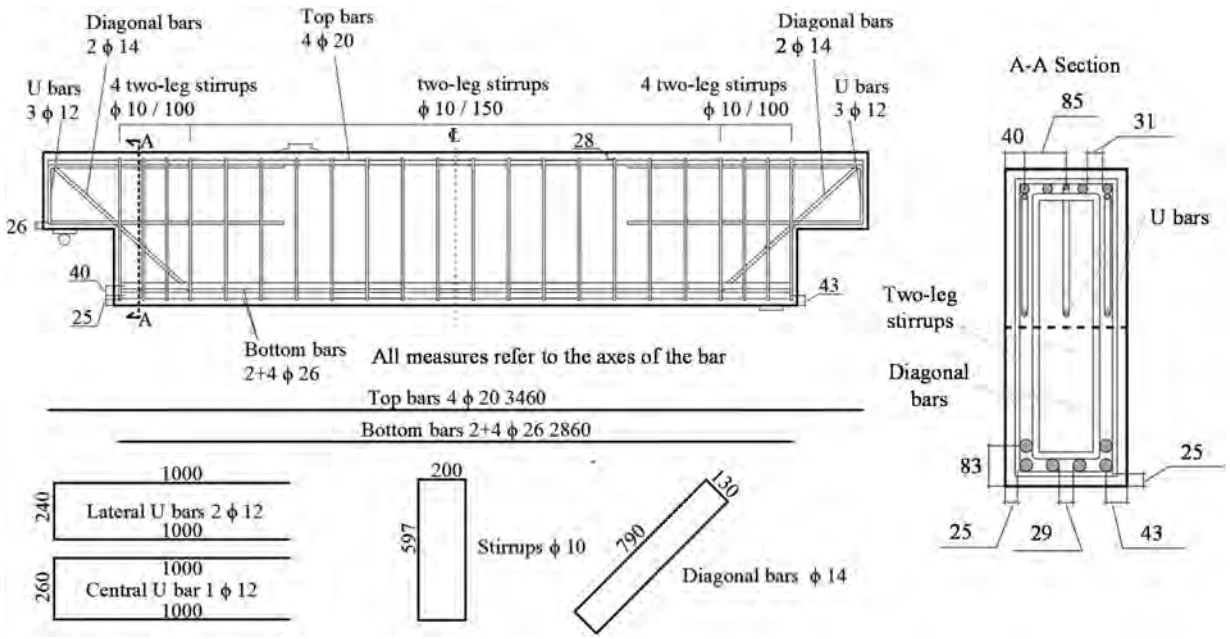

FIGURE 2 Reinforcements of the dapped-end beam. Dimensions in mm. *Source:* Adapted from Reference 48.

parts from their anchorage zones could compromise the tie resistance, the bond stress–slip behavior in these zones is carefully simulated in Section 2.2.3.

Figure 3 shows the instrumentation layout adopted for the dapped-end beam. Four potentiometric displacement transducers and one linear variable displacement transducer (LVDT) are used to measure the load versus crack opening displacement (COD) curves at the horizontal and inclined locations (COD 1, COD 4, LVDT) and load versus COD curves at the vertical locations nearby the nib (COD 2 and COD 3). Two wire deformometers were placed below the dapped-end to measure the load versus vertical displacement curves (at positions D1 and D2).

The mechanical properties of concrete are reported in Table 1. The experimental mean values of compressive and tensile strengths, f_{cm} and f_{ctm}, were measured

17517648, 2024, 2, Downloaded from https://onlinelibrary.wiley.com/doi/10.1002/suco.202301020 by University Degli Studi Di Parma Settore Biblioteche, Wiley Online Library on [15/05/2024]. See the Terms and Conditions (https://onlinelibrary.wiley.com/terms-and-conditions) on Wiley Online Library for rules of use; OA articles are governed by the applicable Creative Commons License

by means of compression and indirect tensile tests, respectively.

The additional mechanical properties are the elastic modulus of concrete E_{cm}, the mass density ρ, the Poisson's ratio ν, the fracture energy in tension, $G_F = 73 \cdot f_{cm}^{0.18}$, and in compression, $G_C = 250 \cdot G_F$, and the total shrinkage ε_{cs}, evaluated according to the Model Code 2010[51] and the Guidelines for Nonlinear Finite Element Analysis of Concrete Structures.[52,53] The experimental mean values of yield and ultimate strengths of reinforcing bars, $f_{sy,0}$ and $f_{su,0}$, and ultimate strain, $\varepsilon_{su,0}$, were measured by means of tensile tests and are reported in Table 2. The modulus of elasticity of steel, E_S, is equal to 210,000 N/mm^2.

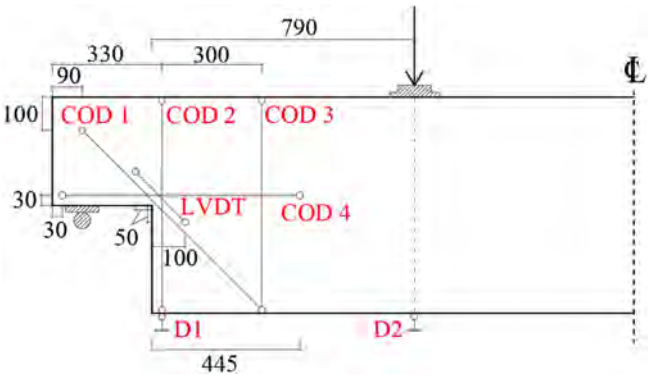

FIGURE 3 Instrumentation layout of the dapped-end beam. Dimensions in mm. *Source:* Adapted from Reference 48.

TABLE 1 Mechanical properties of concrete.

Property	Value	Unit
f_{cm}	48.62	N/mm^2
f_{ctm}	3.73	N/mm^2
E_{cm}	33,000.00	N/mm^2
ρ	2500.00	kg/m^3
ν	0.20	–
G_F	0.104	N/mm
G_C	25.97	N/mm
ε_{cs}	0.00025	–

2.2 | Finite element modeling of the uncorroded dapped-end beam

This section describes the finite element modeling of the uncorroded dapped-end beam. The numerical analyses are carried out by using ABAQUS software.[54] Firstly, the finite element mesh and the boundary conditions are presented. Secondly, the uncorroded material properties and the bond-slip modeling are described.

2.2.1 | Finite element mesh and boundary conditions

The beam is modeled by adopting 8-node multi-layered shell elements with a reduced Gaussian integration scheme (S8R); the average element size is equal to 25 mm (Figure 4). The thickness of the shell elements is subdivided in 11 layers to place the reinforcement at the correct positions and three Simpson's integration points are used for each layer. The external layers are 20 mm thick and represent the concrete cover, while the inner layers have different thicknesses depending on the diameter of the enclosed reinforcement. The applied boundary conditions are represented in Figure 4.

Rebars and stirrups are modeled using both smeared and discrete modeling approaches:

- In the central zone of the beam, smeared reinforcements are used, by assuming perfect bond conditions (Figure 5a).
- In the correspondence of the dapped-ends, a discrete modeling approach for rebars and stirrups (modeled with 3 nodes truss elements T3D2) is used (Figure 5b). In this case, the slip of the reinforcement with respect to the concrete elements is simulated.

A detail of the reinforcement modeled by the discrete approach is shown in Figure 5c. The interaction between reinforcing bars (truss elements) and concrete (shell elements) is modeled by nonlinear spring elements.

TABLE 2 Mechanical properties of uncorroded reinforcing steel.

Reinforcement	$f_{sy,0}$ [N/mm^2]	$f_{su,0}$ [N/mm^2]	$\varepsilon_{su,0}$ [%]
Stirrups, Ø10	526.50	623.70	7.50
U bars, Ø12	530.20	628.20	12.50
Diagonal bars, Ø14	507.70	627.50	9.50
Top bars, Ø20	555.00	677.70	10.90
Bottom bars, Ø26	522.70	634.70	12.10

17517648, 2024, 2, Downloaded from https://onlinelibrary.wiley.com/doi/10.1002/suco.202301020 by University Degli Studi Di Parma Settore Biblioteche, Wiley Online Library on [15/05/2024]. See the Terms and Conditions (https://onlinelibrary.wiley.com/terms-and-conditions) on Wiley Online Library for rules of use; OA articles are governed by the applicable Creative Commons License

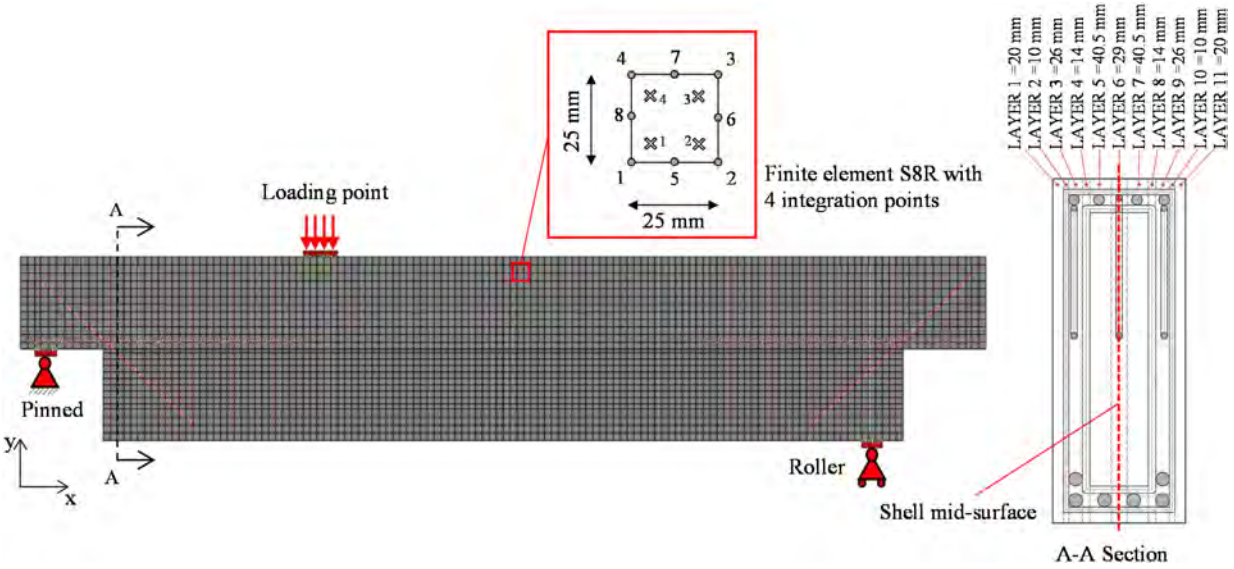

FIGURE 4 Finite element mesh of the dapped-end beam.

The nonlinear behavior of spring elements parallel to the reinforcement axis (local direction 1) is based on the bond stress–slip (τ_b–s) relationship proposed by Model Code 2010,[51] as described in Section 2.2.3. To transform the bond stress–slip relationship into the force–displacement relationship, which characterizes the nonlinear response of the spring elements parallel to the reinforcement axis, constant bond stress along the length of truss elements is assumed. Therefore, the force F is calculated as $F = \alpha\pi\phi L\tau_b$, where ϕ is the bar diameter, L is the length of the truss element, and α is equal to 1/6 for the two outer nodes and equal to 2/3 for the node in the middle of the three-node truss element. The modeling of the nonlinear behavior of the spring elements is considered relevant for the anchorage of the straight horizontal part of the U-shaped bars, placed at the intrados of the nib, because the slip at the anchorage could compromise the tie resistance. Furthermore, the bond stress versus slip behavior is considered relevant also for the inclined, diagonal, and vertical stirrups placed in the cracked zones, since it controls the crack width. Linear elastic behavior is adopted for spring elements perpendicular to the reinforcement axis (local directions 2 and 3) with high stiffness ($K = 10^6$ N/mm). Similarly, the perfect bond is considered in the welded/anchored regions, represented in red in Figure 5b.

For the loading and support steel plates, 8-node multi-layer shell elements (S8R) with a reduced Gaussian integration scheme are used (Figure 5a). The contact along the normal direction (y-axis) between the steel plates and the dapped-end beam is modeled by spring elements characterized by a linear behavior and high stiffness ($K = 10^6$ N/mm). No interface elements were modeled along the x-axis to avoid stress localizations due to shear stresses transmitted at the contact between the steel plates and the dapped-end beam. Therefore, to avoid differential displacements between the steel plates and the dapped-end beam, a constraint is defined by imposing equal horizontal displacements at the nodes located at the mid-length of the steel plates and the closest nodes of the dapped-end beam. The translations along the x and y axes at a single node of the left steel plate are constrained as well as the translation along y-axis at a single node of the right steel plate. A linear elastic behavior is assumed for the loading and supporting steel plates by assigning an elastic modulus of 200,000 N/mm^2 and a Poisson's ratio of 0.3. The NLFE analyses are carried out as follows:

- In the first step, the gravity load is applied by assigning a concrete density $\rho = 2500$ kg/m^3.
- In the second step, an increasing vertical displacement is applied as a boundary condition to all the nodes placed at the extrados of the loading steel plate.

The regular Newton–Raphson method is used to solve the nonlinear problem.

2.2.2 | Mechanical properties of concrete and reinforcement steel

The reinforced concrete is modeled by means of the PARC_CL 2.1 crack model,[43,44] a total strain fixed-crack model with smeared reinforcement, implemented in the user subroutine of the ABAQUS software. In the regions

17517648, 2024, 2, Downloaded from https://onlinelibrary.wiley.com/doi/10.1002/suco.202301020 by University Degli Studi Di Parma Settore Biblioteche, Wiley Online Library on [15/05/2024]. See the Terms and Conditions (https://onlinelibrary.wiley.com/terms-and-conditions) on Wiley Online Library for rules of use; OA articles are governed by the applicable Creative Commons License

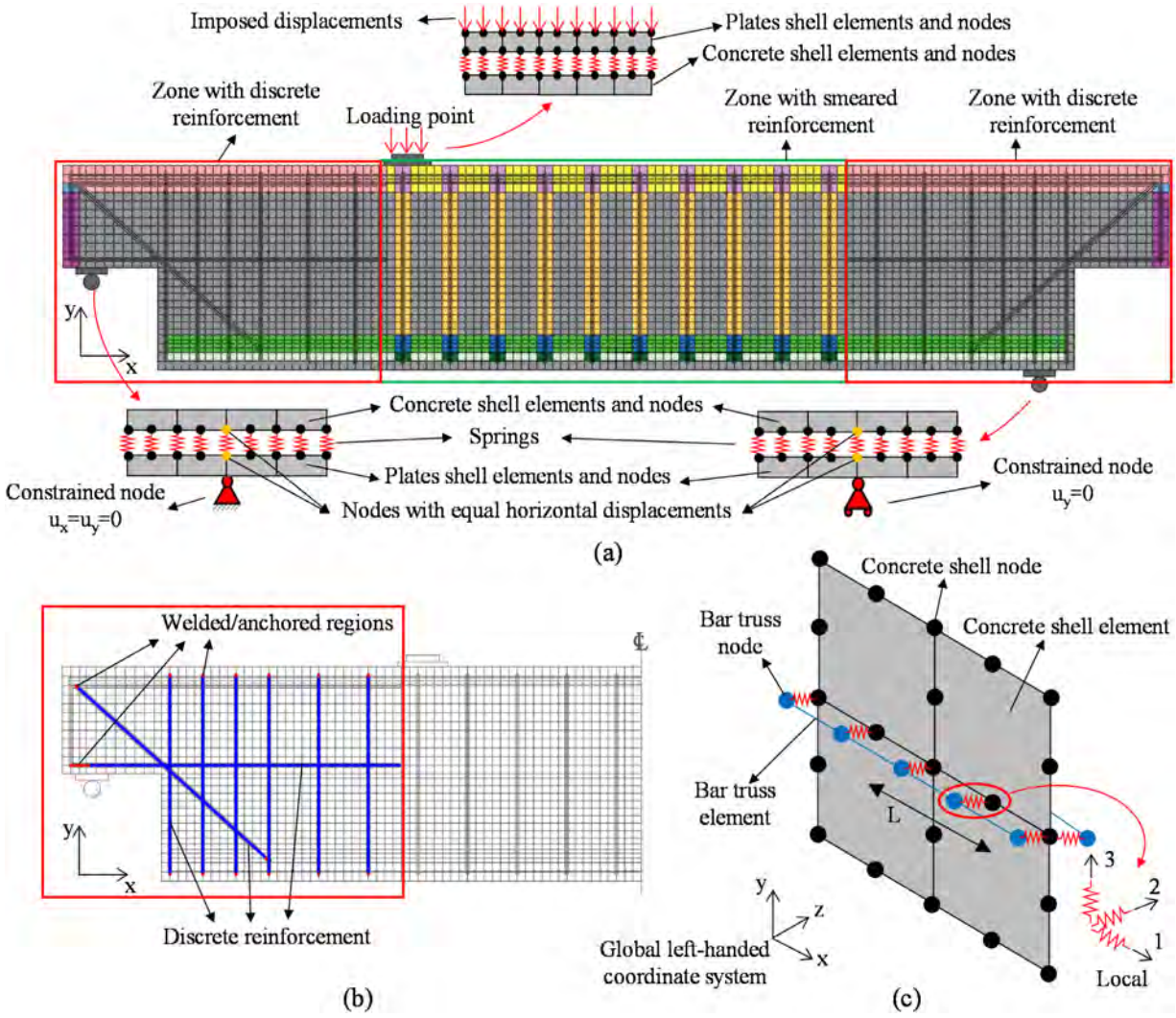

FIGURE 5 (a) Smeared and discrete FE modeling zones, (b) detail of reinforcement modeled with discrete approach, and (c) detail of the interaction between discrete reinforcement and concrete elements. FE, finite element.

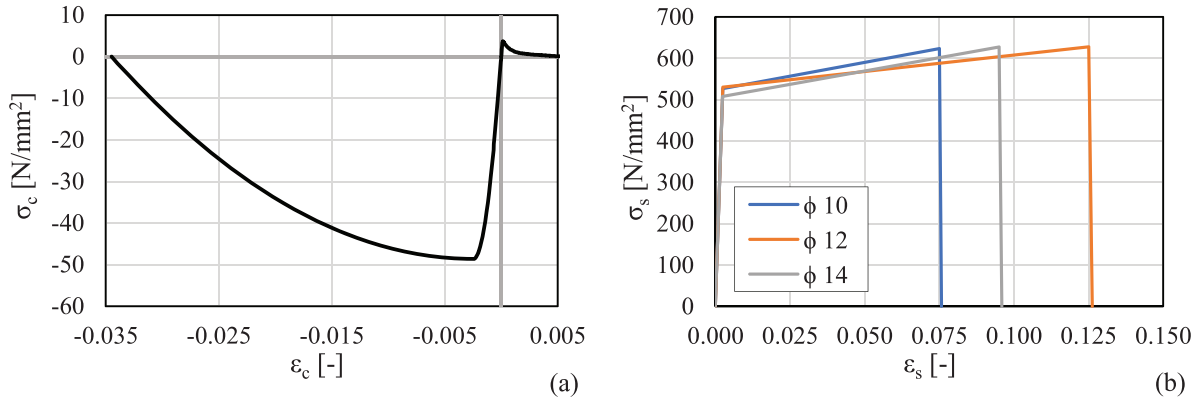

FIGURE 6 (a) Tensile and compressive envelope curves for concrete. (b) Stress–strain laws adopted for steel reinforcement.

of the beam where the reinforcements are modeled with a discrete approach, the PARC_CL 2.1 crack model is used to describe the behavior of concrete only. The PARC_CL 2.1 crack model is suitable for monotonic, cyclic, and dynamic analyses. Because it considers for the opening and closing of adjacent cracks, the PARC_CL 2.1

17517648, 2024, 2, Downloaded from https://onlinelibrary.wiley.com/doi/10.1002/suco.202301020 by University Degli Studi Di Parma Settore Biblioteche, Wiley Online Library on [15/05/2024]. See the Terms and Conditions (https://onlinelibrary.wiley.com/terms-and-conditions) on Wiley Online Library for rules of use; OA articles are governed by the applicable Creative Commons License

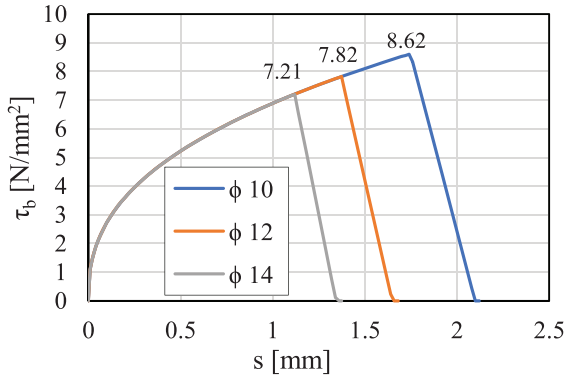

FIGURE 7 Bond stress versus slip laws defined according to Model Code 2010[51] for different bar diameters.

crack model is a useful tool also for monotonically loaded members. The reader is referred to References 43,44,55 for more details.

Figure 6a shows the tensile and compressive envelope curves for concrete, while Figure 6b shows the constitutive laws adopted for steel reinforcement. The input parameters of the model, required for the evaluation of the stiffness matrix and the stress field at each integration point, are reported in Table 1 and Table 2.

2.2.3 | Bond–slip behavior

The bond–slip behavior is simulated by spring elements, which are used to connect the truss elements—modeling the discrete reinforcement—to the multilayer shell elements. The spring elements have a linear behavior along the axis perpendicular to the reinforcement direction (directions 2 and 3 in Figure 5c) and nonlinear behavior along the axis parallel to the reinforcement direction (direction 1 in Figure 5c). Specifically, a stiffness of 10^6 N/mm is assigned to linear spring elements, while the bond stress versus slip law proposed by Model Code 2010[51] is used to define the nonlinear behavior of nonlinear spring elements. Figure 7 shows the bond stress versus slip curves (τ_b–s) with the maximum value at the peak τ_{bu}, adopted for the different reinforcements—calculated assuming splitting failure, unconfined concrete, and no good bond conditions—for different diameters of rebars modeled by adopting the discrete approach.

2.3 | Results of NLFE analyses of uncorroded dapped-end beam

Figure 8 shows the comparison between experimental measurements and NLFEA results, which are in good agreement.

The experimental measurements of the inclined LVDT shown in Figure 3, which are assumed to correspond to the crack opening width values, are compared with the relative displacements of the nodes of the mesh placed in correspondence of the connection of the LVDT extremities to the faces of the beam. The ultimate values of the LVDT measurements are lower than the NLFEA results because, to preserve the LVDT, the device was removed before failure, in correspondence with a critical value of the damage registered in the dapped-end beam. Figure 8a shows the load versus crack width curve of the numerical determined sequence of events, which allows the reader to understand the resisting mechanism of the dapped-end beam.

First, an inclined crack develops at the re-entrant corner (point 1), followed by the yielding of the diagonal reinforcement (point 2), the first stirrup (point 3), and the U-bars (point 4). The curve then bends significantly and the second and third stirrups yield at points 5 and 6 respectively. Finally, the collapse of the dapped-end beam occurs due to the rupture of the first vertical stirrup (point 8). Figure 9 shows the comparison between the experimental crack pattern at failure and the numerical one, where the contour represents the crack opening width values obtained by NLFE analysis. The crack pattern during loading is characterized by the following events: (i) an inclined crack develops at the re-entrant corner (position 1 in Figure 9b), (ii) a vertical crack forms at the intrados of the beam under the applied load, followed by a series of inclined cracks that gradually form with increasing opening width values (position 2 in Figure 9b), and (iii) the formation of a horizontal crack at the top of the dapped-end beam is recorded at failure (position 3 in Figure 9b).

No anchorage failure of U-shaped straight parts is observed. Figure 10 shows the trend of bond stress and slip (Figure 10b) along the length of U-bars at maximum load. In the left part, the rebars are anchored along the nib of the dapped-end beam, therefore the initial part of them is considered to be fixed (red in Figure 10b) and is not reported in the charts (the rebar axis starts from 75 mm). It can be observed that, in general, in the zone characterized by higher values of crack opening width and multiple cracks (as shown in Figure 9 and in Figure 10a where the background is shaded light blue), the values of the bond stress vary between positive and negative values with a frequency that depends on the crack spacing, whereas in the zone characterized by lower values of crack opening width and spaced cracks (as illustrated in Figure 9 and in Figure 10a where the background is shaded light pink), the values of the bond stress are more regular and

17517648, 2024, 2, Downloaded from https://onlinelibrary.wiley.com/doi/10.1002/suco.202301020 by University Degli Studi Di Parma Settore Biblioteche, Wiley Online Library on [15/05/2024]. See the Terms and Conditions (https://onlinelibrary.wiley.com/terms-and-conditions) on Wiley Online Library for rules of use; OA articles are governed by the applicable Creative Commons License

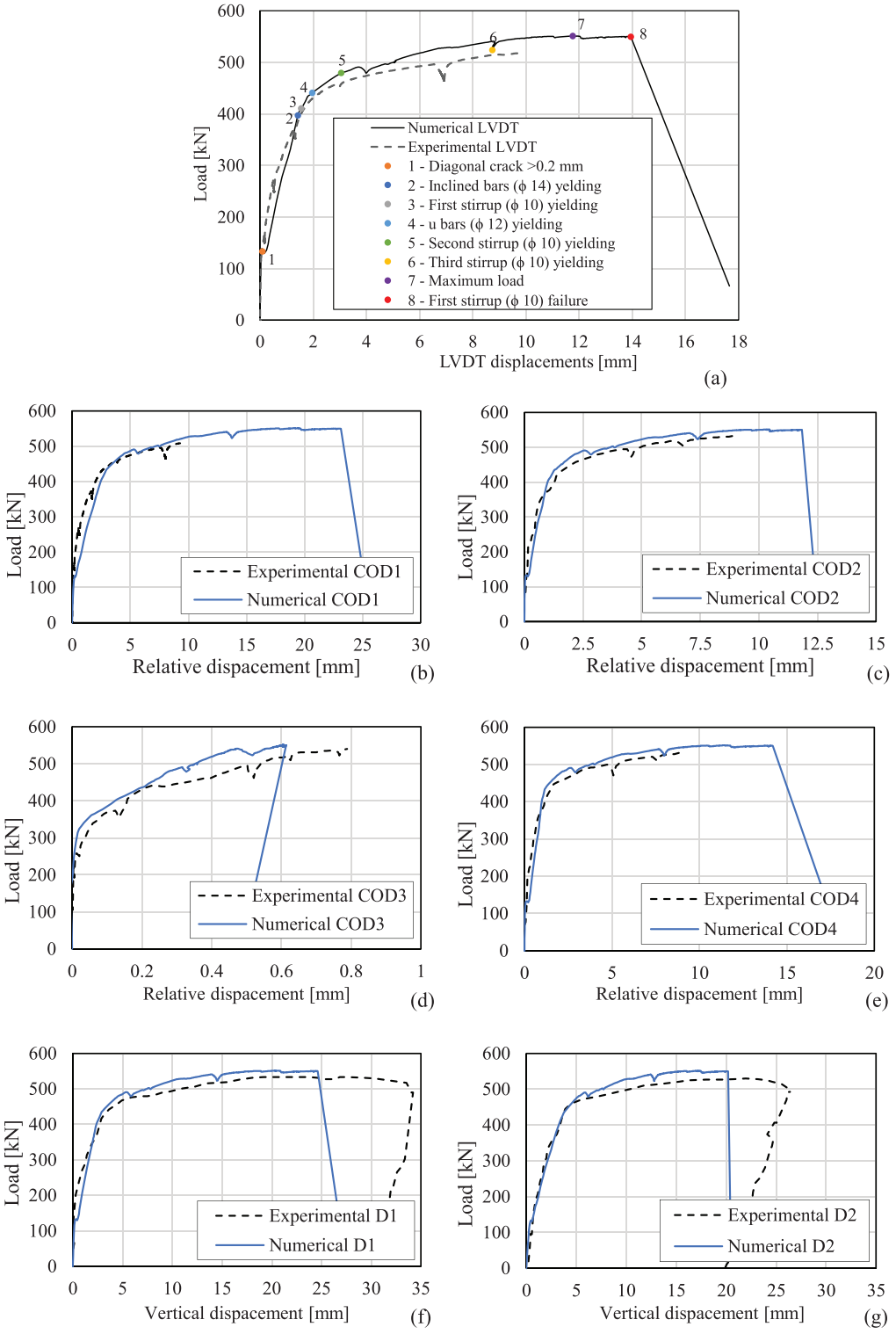

FIGURE 8 Comparison between experimental and NLFEA results: (a) load–LVDT; (b) load–COD1; (c) load–COD2; (d) load–COD3; (e) load–COD4; (f) load–D1; (g) load–D2.

continuous along the length of the bar. It can be concluded that, the length of the U-bars is sufficient to avoid anchorage failure (Figure 10a) because the bond stress cannot reach the value of the bond strength, which is equal to 7.82 MPa, as shown in Figure 7. Thus, although the NLFE approach can detect anchorage failure, it was not observed in the case study analyzed.

17517648, 2024, 2, Downloaded from https://onlinelibrary.wiley.com/doi/10.1002/suco.202301020 by University Degli Studi Di Parma Settore Biblioteche, Wiley Online Library on [15/05/2024]. See the Terms and Conditions (https://onlinelibrary.wiley.com/terms-and-conditions) on Wiley Online Library for rules of use; OA articles are governed by the applicable Creative Commons License

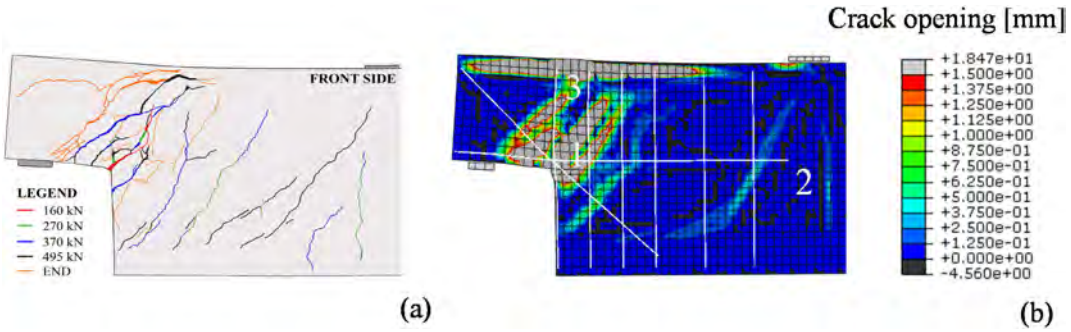

FIGURE 9 Comparison between (a) experimental[48] and (b) NLFEA crack patterns at failure.

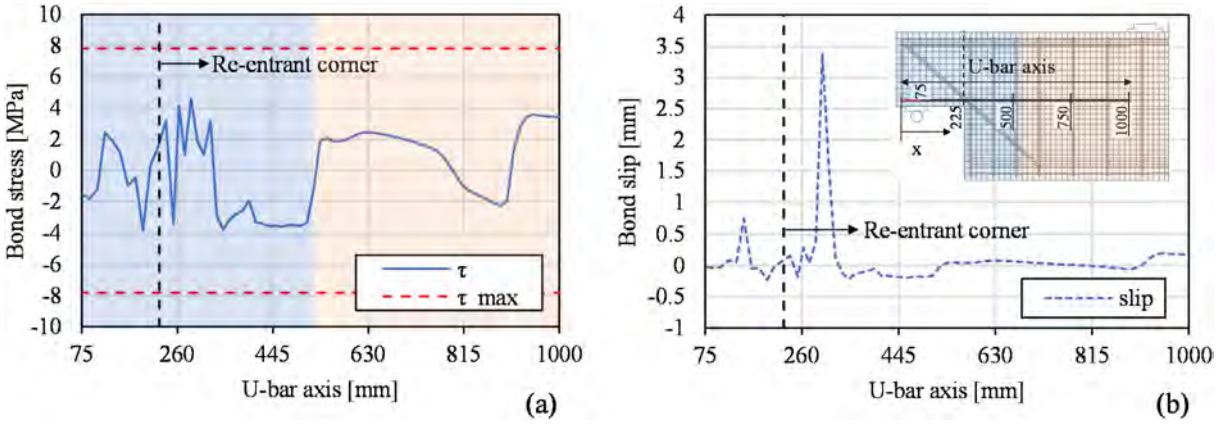

FIGURE 10 (a) Bond stress and (b) bond slip along the U-bars at ultimate load.

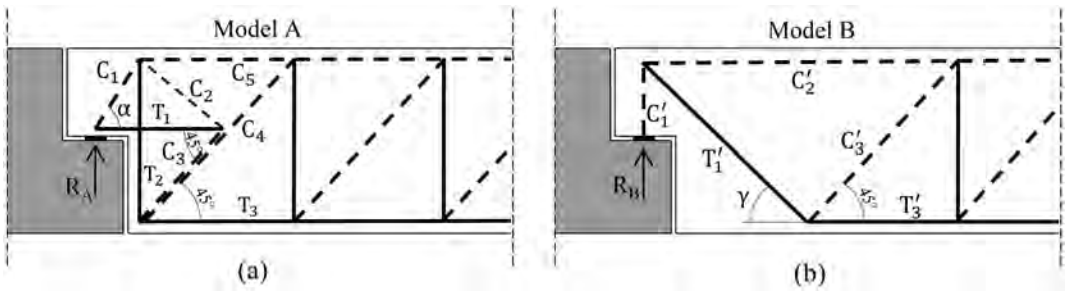

FIGURE 11 Strut-and-tie Model A (a) and Model B (b) provided by Eurocode 2.[11]

2.4 | S&T method for uncorroded dapped-end beam

The results of NLFE models were compared with those obtained with S&T method proposed by the Eurocode 2[11] and used to design the beam. Eurocode 2[11] recommends two models for the analytical calculations shown in Figure 11a and Figure 11b, named Model A and Model B, where the struts are labeled "C" (dotted lines) and the ties labeled "T" (continuous lines).

To verify the correspondence of the truss position and inclination with the NLFEA results, Figure 12 shows the evolution of the minimum principal stress at the first cracking load and at the ultimate load. The minimum principal stress field clearly shows that both S&T models contribute to the total capacity. Model B, associated with the first mechanism, is activated at low load levels (the diagonal bars yield before the stirrups and the U-shaped bar), while Model A better reflects the behavior of the dapped-end beam at failure. The minimum principal stress field (Figure 12) reveals that the strut C_2 in Model A does not form, therefore the equilibrium at node 1 is allowed by the anchorage force of the horizontal bar, and the struts C_2 and C_3 should be canceled.

17517648, 2024, 2, Downloaded from https://onlinelibrary.wiley.com/doi/10.1002/suco.202301020 by University Degli Studi Di Parma Settore Biblioteche, Wiley Online Library on [15/05/2024]. See the Terms and Conditions (https://onlinelibrary.wiley.com/terms-and-conditions) on Wiley Online Library for rules of use; OA articles are governed by the applicable Creative Commons License

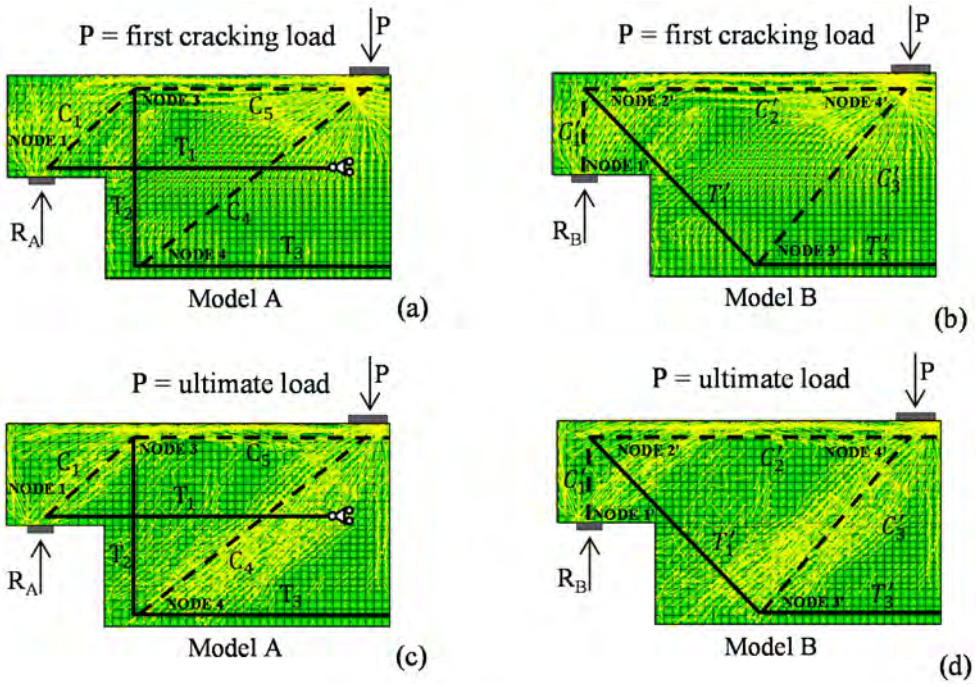

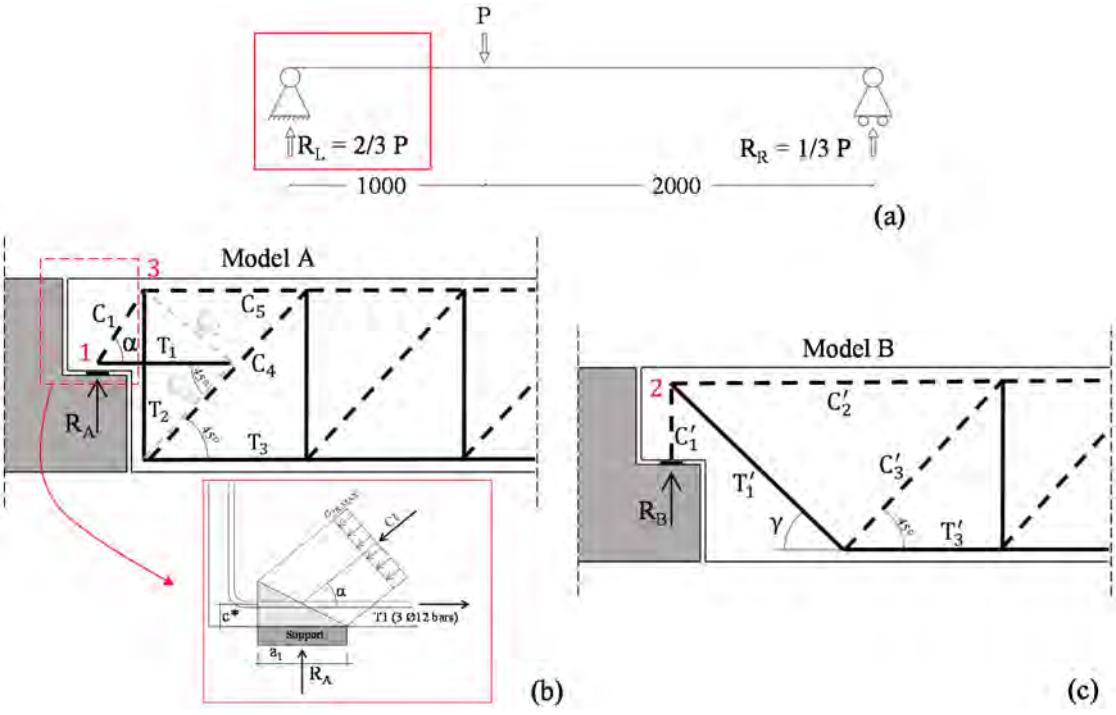

FIGURE 12 Comparison of NLFEA minimum principal stress field and strut-and-tie Models A and B at first cracking load (a and b) and ultimate load (c and d).

FIGURE 13 (a) Static scheme of the dapped-end beam. (b) Strut-and-tie model for at the left support. (c) CCT Node 1.

The ultimate load capacity $P_{ult,A}$ of Model A is obtained with the Equation (1) considering the minimum of the following resistances:

$$P_{ult,A} = \frac{3}{2}\min[R_{1A}, R_{2A}, R_{3A}]. \quad (1)$$

The coefficient 3/2 is used to consider the static scheme of the test and relates the left reaction R_L to the maximum load P applied to the beam (Figure 13a). The resistance R_{1A} is related to the compression strength in the strut C_1, and it is evaluated with Equation (2) by considering the vertical equilibrium at node 1 (Compression-Compression-Tension,

17517648, 2024, 2, Downloaded from https://onlinelibrary.wiley.com/doi/10.1002/suco.202301020 by University Degli Studi Di Parma Settore Biblioteche, Wiley Online Library on [15/05/2024]. See the Terms and Conditions (https://onlinelibrary.wiley.com/terms-and-conditions) on Wiley Online Library for rules of use; OA articles are governed by the applicable Creative Commons License

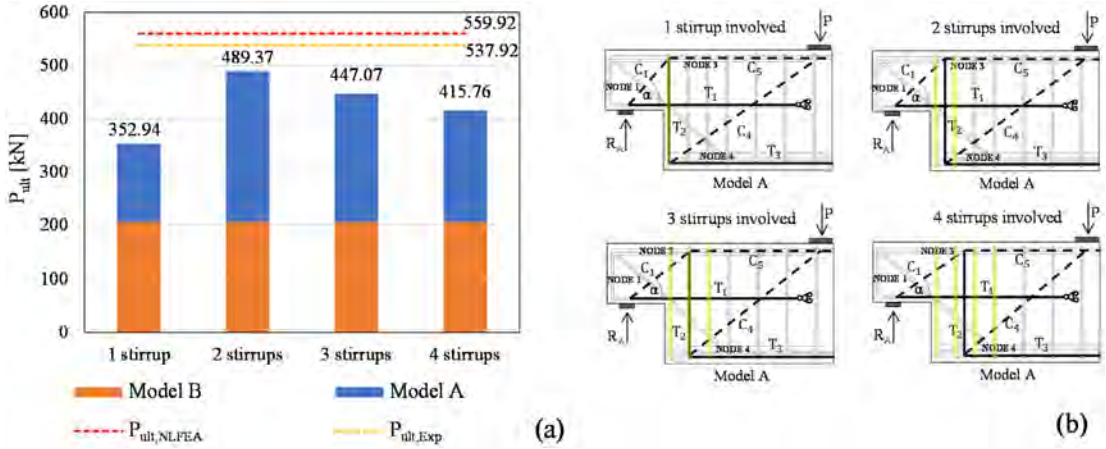

FIGURE 14 (a) Result of strut-and-tie method for uncorroded beams considering different number of stirrups in tie T_2; (b) position of the tie T_2 as function of the number of stirrups involved.

CCT type), where the thickness of the strut is evaluated by geometrical considerations starting from the length of the support and the reinforcement in the node (Figure 13b).

$$\begin{aligned} R_{1A} &= C_1 \cdot \sin(\alpha) \\ &= [(a_1 \cdot \sin(\alpha) + 2c^* \cdot \cos(\alpha)) \cdot b \cdot \sigma_{Rd,Max}] \cdot \sin(\alpha), \end{aligned} \tag{2}$$

where a_1 is the length of the support, c^* the distance between bar axis of the tie and the base of the node, b the width of the beam, and $\sigma_{Rd,Max} = k_2 \nu' f_{cm} = 0.71 \cdot f_{cm}$ is the reduced concrete compressive strength for CCT nodes according to Eurocode 2.[11] The angle α represents the inclination of the strut C_1, depending on the tie T_1, whose position corresponds to the centreline of the stirrups involved in the resisting mechanism.

The resistance of the tie T_1 is evaluated by considering the horizontal equilibrium at the Node 1 by using the tensile strength of the U-bars according to Equation (3):

$$R_{2A} = T_1 \cdot \tan\alpha = \left[3 \cdot A_{S,\phi 12} \cdot f_{su,0,\phi 12}\right] \cdot \tan\alpha, \tag{3}$$

where $A_{S,\phi 12}$ is the area of a bar ϕ12 and $f_{su,0,\phi 12}$ is the uncorroded ultimate tensile strength of the bars. Finally, the resistance of the tie T_2 is evaluated by considering the resistance that can be developed by the stirrups considering the vertical equilibrium at Node 3 and then in the Node 1, as given by Equation (4):

$$R_{3A} = n \cdot 2 \cdot A_{S,\phi 10} \cdot f_{su,0,\phi 10}, \tag{4}$$

where n is the number of stirrups with two legs considered in the calculations, $A_{s,\phi 10}$ is the area of a singular bar ϕ10, and $f_{su,0,\phi 10}$ is the uncorroded ultimate tensile strength of the stirrups.

The ultimate load capacity for the Model B is calculated by considering the resistance of the tie T_1'. The vertical equilibrium at Node 2 allows to evaluate the resistance as follows with Equation (5):

$$P_{ult,B} = \frac{3}{2} T_1' \cdot \sin\gamma = \frac{3}{2}\left[2 \cdot A_{S,\phi 14} \cdot f_{su,0,\phi 14}\right] \cdot \sin\gamma, \tag{5}$$

where $A_{s,\phi 14}$ is the area of a singular bar ϕ14 and $f_{su,0,\phi 14}$ is the uncorroded ultimate tensile strength of bar ϕ14. The angle γ represents the inclination of the tie T_1' (i.e., the diagonal bars), depending on the geometrical features. To ensure that the failure is attributed to the rupture of inclined bars (T_1'), it has been verified that the ties corresponding to longitudinal bars (T_3') and the struts (C_1', C_2', C_3') have greater resistances. Finally, the total ultimate load capacity of the dapped-end beam is obtained by summing the resistances of the two models A and B with Equation (6):

$$P_{ult} = P_{ult,A} + P_{ult,B}. \tag{6}$$

It should be noted that for the ultimate load capacity Model A it is possible to consider different numbers of stirrups (from 1 to 4) involved in the calculation of the tie resistance T_2. In fact, the number of stirrups influences the position and the resultant of the tie T_2. In particular, the angle of inclination (α) of the strut C_1 decreases and node 3 is shifted to the right as the number of stirrups involved in the resistance mechanism increases (Figure 14b).

A comprehensive comparison of the capacity of the analyzed dapped-ends beam is shown in Figure 14a;

17517648, 2024, 2, Downloaded from https://onlinelibrary.wiley.com/doi/10.1002/suco.202301020 by University Degli Studi Di Parma Settore Biblioteche, Wiley Online Library on [15/05/2024]. See the Terms and Conditions (https://onlinelibrary.wiley.com/terms-and-conditions) on Wiley Online Library for rules of use; OA articles are governed by the applicable Creative Commons License

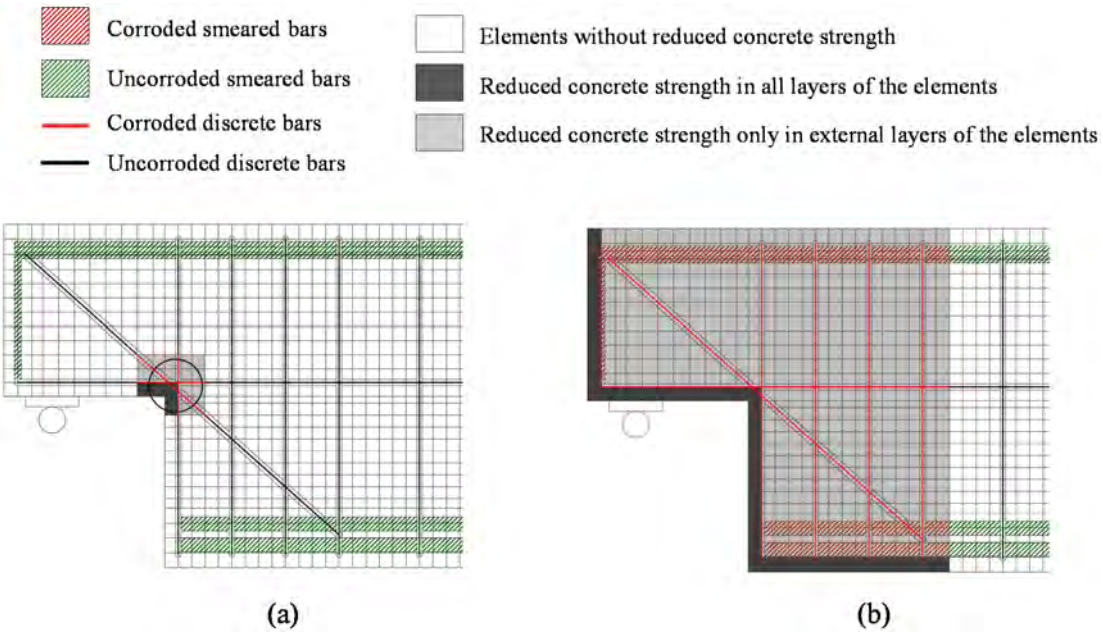

FIGURE 15 Corrosion scenarios: (a) S1-localized corrosion and (b) S2-global corrosion.

the results confirm that the S&T method provides conservative estimations compared to NLFEA and experimental tests.

The capacity of the analyzed dapped-ends-beam is finally evaluated by assuming two stirrups for Model A. This choice is also motivated from the NLFE results. In fact, Figure 22a shows that the highest values of plastic strain are achieved by Stirrups 1 and 2; Stirrup 3 does not achieve relevant plastic strain while Stirrup 4 remains in the elastic stage.

On the one hand, Figure 14a shows that the highest resistance can be obtained by the S&T method when the ultimate strength f_t is used to calculate the tensile resistance of the tie. On the other hand, Figure 22 shows that at failure not all the reinforcements—characterized by different diameters—reach their ultimate strain. Therefore, special care must be taken when adopting the ultimate strength of the ties. A more conservative assessment using the yield strength is suggested by the authors and most Codes and Guidelines (such as the Model Code 2010[51]) were reducing coefficients are also proposed when the capacity is obtained by adding the resistances of two or more truss models.

3 | SIMULATED CORROSION SCENARIOS AND SIMPLIFIED S&T METHOD

In this section, the previous finite element model has been extended with the introduction of corrosion. Firstly, the selected corrosion scenarios and associated parameters are reported and discussed. Secondly, the corroded material properties are described. Finally, the results obtained are presented. It should be considered that the assumptions for the FE modeling described in Section 2.2 are still valid.

3.1 | Corrosion scenarios and parameters

3.1.1 | Corrosion scenarios

Based on observations in the literature,[56–58] two different corrosion scenarios are considered:

- A localized corrosion in a region of the dapped-end beam more prone to water stagnation—called "Scenario 1" (S1).
- A global corrosion in the external faces of the dapped-end beam—called "Scenario 2" (S2).

In Scenario 1 (Figure 15a), according to Desnerck et al.,[56] it is assumed that corrosion is localized in the re-entrant corner of the dapped-end in a zone encompassing an inscribed circle of 100 mm diameter (Figure 15a). This region is critical because it corresponds to the position where the first cracks form, potentially exposing the rebars to aggressive agents such as chlorides. Figure 15a shows: (i) the portion of the rebar subject to corrosion in red, (ii) the concrete cover elements (gray elements) where the

17517648, 2024, 2, Downloaded from https://onlinelibrary.wiley.com/doi/10.1002/suco.202301020 by University Degli Studi Di Parma Settore Biblioteche, Wiley Online Library on [15/05/2024]. See the Terms and Conditions (https://onlinelibrary.wiley.com/terms-and-conditions) on Wiley Online Library for rules of use; OA articles are governed by the applicable Creative Commons License

compressive strength is reduced to account for splitting cracks (see Section 3.2.1). In Scenario 2 (Figure 15b), it is assumed that corrosion affects a wide external part of the dapped-end beam and the corroded bars are shown in red. To account for splitting cracks in the concrete cover, the compressive strength is reduced similarly to the previous scenario, as shown in Figure 15b.

3.1.2 | Parameters for chloride-induced corrosion

To investigate the dependence of the load carrying capacity of dapped-ends on the extension and on the level of the damage induced by corrosion, several periods of corrosion propagation, t_p, were analyzed for these two different corrosion scenarios. The model proposed by Tuutti[59] was adopted. An exposure class XD3[11] was chosen because the dapped-ends of bridge beams are usually exposed to wet and dry cycles and to chlorides from deicing agents. The analyses of dapped-end beams have been carried out considering only the propagation period t_p (the initiation period is not considered). The corrosion induced by chloride exposure is characterized by local damage, usually measured in terms of the pit depth. Indeed, the pit depth as a function of propagation time, $p(t_p)$ (in mm/year), is defined according to the CONTECVET manual[60] with Equation (7):

$$p(t_p) = 0.0116 \cdot I_{corr} \cdot t_p \cdot \alpha_p, \tag{7}$$

where I_{corr} is the corrosion rate (in μA/cm^2), t_p is the propagation time after corrosion initiation, and α_p is a coefficient which considers the different corrosion types and for pitting is assumed to be 10. The value of the corrosion rate I_{corr} depends on the exposure classes of EN 206-1[61] and, according to table 5.4 of the CONTECVET manual,[60] the value ranges between 0.5 and 5 μA/cm^2.

To demonstrate that the damage detection alone is not sufficient for predicting the residual service life and that corrosion rate must be carefully measured for a proper estimation of the effects of the aggressive environment over time, in the present work two different corrosion rates are analyzed: (i) the first called "low corrosion rate" (LCR) with a $I_{corr} = 0.5$ μA/cm^2 and (ii) the second called "medium corrosion rate" (MCR) with $I_{corr} = 2.5$ μA/cm^2. The cross-sectional area of a pit, $A_p(t_p)$, can be evaluated according to the model proposed by Val,[62] by assuming a hemispherical geometry of the pit (Figure 16). Based on this model, the cross-sectional area of a pit $A_p(t_p)$—in a rebar of diameter D_0 after t_p years of corrosion propagation—can be calculated as given by Equations (8)–(13):

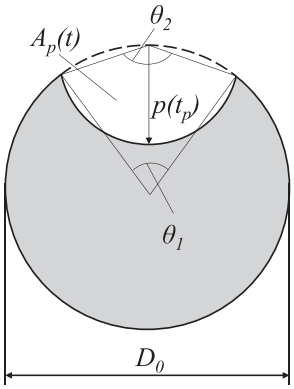

FIGURE 16 Hemispherical geometry of pitting in a corroded reinforcing bar.[62]

$$A_p(t_p) = \begin{cases} A_1 + A_2 & p(t_p) \le \dfrac{D_0}{\sqrt{2}} \\ \dfrac{\pi D_0^2}{4} - A_1 + A_2 & \dfrac{D_0}{\sqrt{2}} < p(t_p) \le D_0, \\ \dfrac{\pi D_0^2}{4} & p(t_p) > D_0 \end{cases} \tag{8}$$

where the previous parameters are calculated as follows:

$$A_1 = 0.5\left[\theta_1\left(\frac{D_0}{2}\right)^2 - a\left|\frac{D_0}{2} - \frac{p(t_p)^2}{D_0}\right|\right], \tag{9}$$

$$A_2 = 0.5\left[\theta_2 p(t)^2 - a\frac{p(t_p)^2}{D_0}\right], \tag{10}$$

$$a = 2p(t)\sqrt{1 - \left[\frac{p(t_p)}{D_0}\right]^2}, \tag{11}$$

$$\theta_1 = 2\arcsin\left(\frac{a}{D_0}\right), \tag{12}$$

$$\theta_2 = 2\arcsin\left(\frac{a}{2p(t_p)}\right). \tag{13}$$

Based on the cross-sectional area of a pit, $A_p(t_p)$, the section loss, $\mu(t_p)$, can be calculated with Equation (14), according to[15]:

$$\mu(t_p) = \frac{A_p(t_p)}{A_0}, \tag{14}$$

where A_0 is the is transversal cross-sectional area of the uncorroded bar. Due to the different corrosion rates,

17517648, 2024, 2, Downloaded from https://onlinelibrary.wiley.com/doi/10.1002/suco.202301020 by University Degli Studi Di Parma Settore Biblioteche, Wiley Online Library on [15/05/2024]. See the Terms and Conditions (https://onlinelibrary.wiley.com/terms-and-conditions) on Wiley Online Library for rules of use; OA articles are governed by the applicable Creative Commons License

the chosen propagation times are different: for MCR they are equal to 20, 25, 30, 35, and 40 years, while for LCR they are 25, 50, 75, 100, and 125 years. For each propagation time, the following corroded cases are examined in the following paragraphs:

1. Scenario 1 (localized corrosion, Figure 15a) with LCR ($I_{corr} = 0.5$ μA/cm^2), S1-LCR.
2. Scenario 1 (localized corrosion, Figure 15a) with MCR ($I_{corr} = 2.5$ μA/cm^2), S1-MCR.
3. Scenario 2 (global corrosion, Figure 15b) with LCR ($I_{corr} = 0.5$ μA/cm^2), S2-LCR.
4. Scenario 2 (global corrosion, Figure 15b) with MCR ($I_{corr} = 2.5$ μA/cm^2), S2-MCR.

It should be noted that this study did not investigate the spatial variation of the pit depth along bars although the maximum pit depth of each rebar affects its overall mechanical behavior. This aspect should be investigated in future studies.

3.2 | Corroded material properties

3.2.1 | Concrete cover

The expansion of corrosion products causes splitting cracks. In the NLFE model a reduced compressive strength of cracked concrete, $f_{cm,red}(t_p)$, is assigned to the concrete cover according to,[63] expressed with Equation (15):

$$f_{cm,red}(t_p) = \frac{f_{cm}}{\left(1 + 0.1\left(\frac{\sum w_i^{cor}(t_p)}{b}\right)/0.002\right)}, \quad (15)$$

where b is the width of the cracked cross-section and w_i^{cor} is the width of the cracks caused by corrosion,[63] which can be computed with Equation (16):

$$\sum w_i^{cor}(t_p) = 2\pi(\nu_{r,s} - 1)X'_b = 2\pi(\nu_{r,s} - 1)\cdot p(t_p), \quad (16)$$

where $\nu_{r,s} = 2$ is the volumetric expansion ratio of oxides to virgin material, and X'_b is the depth of corrosion attack in the reinforcement and corresponds to $p(t_p)$ computed with Equation (7).

Figure 15 shows the concrete cover elements where the compressive strength is reduced in all the layers that subdivide the thickness of the dapped-ends (dark gray) and the elements where the compressive strength is reduced only in the external layers (light gray). In Scenario 2 (Figure 15b), it is assumed that the area interested by corrosion extends up to the fourth stirrup. The concrete cover at the top of the beam is not affected by corrosion in all layers because usually this portion of beam is protected by the deck above the beam.

3.2.2 | Reinforcing steel

Once the propagation period, t_p, is selected, the corresponding section loss $\mu(t_p)$ can be evaluated. The section loss $\mu(t_p)$ is the input parameter of the assumed stress–strain relationships for corroded reinforcement, as proposed by Chen et al.[15] The stress–strain law of the corroded bar is interrupted at an ultimate stress value, $f_{su,corr}(t_p)$, obtained by considering the equilibrium of uniaxial forces between the minimum cross-section of the corroded bar and the uncorroded cross-section outside the pit (Equation (17)):

$$f_{su,corr}(t_p) = f_{su,0}(1 - \mu(t_p)). \quad (17)$$

The ultimate strain $\varepsilon_{su,corr}(t_p)$ is given by Equation (18): where the subscript "0" stands for uncorroded bars, $E_{sh,0}$ is the tangent slope at the onset of strain-hardening, and $\varepsilon_{sh,0}$ is the strain at the onset of hardening. The term μ_{crit} represents the critical value of the section loss that cause rebar fracture in the elastic stage (i.e., before yielding), and is calculated as given in Equation (19). Equation (20) provides the value of the parameter P to be used in Equation (18).

$$\varepsilon_{su,corr}(t_p) = \begin{cases} \varepsilon_{su,0} - (\varepsilon_{su,0} - \varepsilon_{sh,0})\left(\frac{f_{su,0}}{f_{su,0} - f_{sy,0}}\mu(t_p)\right)^{\frac{1}{P}} & \mu(t_p) < \mu_{crit} \text{ or } f_{sy,0} < f_{su,corr}(t_p) \le f_{su,0} \\ \in [\varepsilon_{sy0}\varepsilon_{sh,0}] & \mu(t_p) = \mu_{crit} \text{ or } f_{su,corr}(t_p) = f_{sy,0} \\ \frac{f_{su,0}\varepsilon_{sy,0}}{f_{sy,0}}(1 - \mu(t_p)) & \mu(t_p) > \mu_{crit} \text{ or } f_{su,corr}(t_p) < f_{sy,0} \end{cases}, \quad (18)$$

17517648, 2024, 2, Downloaded from https://onlinelibrary.wiley.com/doi/10.1002/suco.202301020 by University Degli Studi Di Parma Settore Biblioteche, Wiley Online Library on [15/05/2024]. See the Terms and Conditions (https://onlinelibrary.wiley.com/terms-and-conditions) on Wiley Online Library for rules of use; OA articles are governed by the applicable Creative Commons License

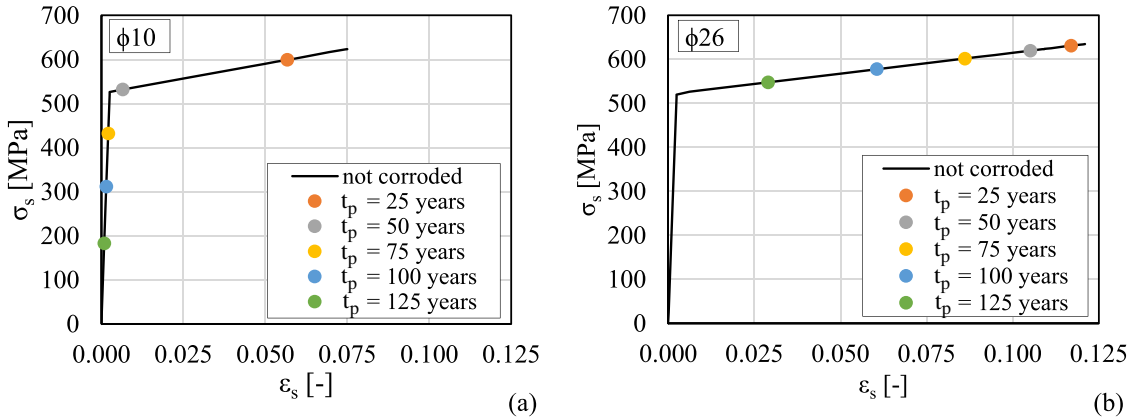

FIGURE 17 Ultimate strain at different propagation times, t_p, calculated in the case of low corrosion rate (LCR) for rebar having diameter (a) $\Phi = 10$ mm and (b) $\Phi = 26$ mm.

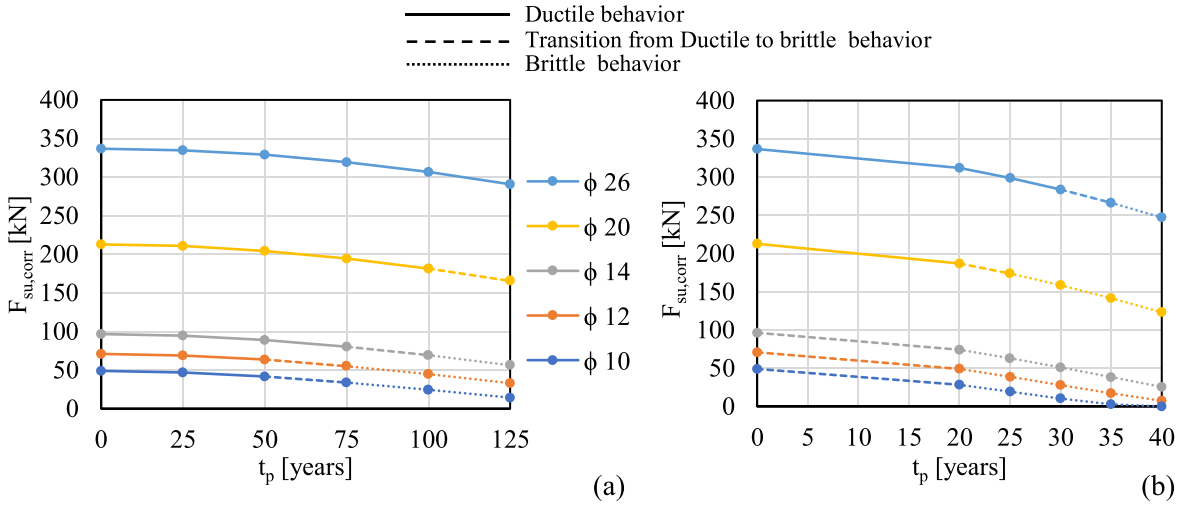

FIGURE 18 Ultimate tensile resistance, $F_{su,corr}(t_p)$, calculated for different values of propagation time, t_p, and for different bar diameters in the case of (a) LCR and (b) MCR. LCR, low corrosion rate; MCR, medium corrosion rate.

$$\mu_{crit} = 1 - \frac{f_{sy,0}}{f_{su,0}}, \tag{19}$$

$$P = E_{sh,0}\frac{\varepsilon_{su,0} - \varepsilon_{sh,0}}{f_{su,0} - f_{sy,0}}. \tag{20}$$

A bilinear stress versus strain law is assumed for corroded bars, therefore $\varepsilon_{sh,0} = \varepsilon_{sy,0}$ and $P = 1$. In Figure 17a and Figure 17b, the ultimate strains, $\varepsilon_{su,corr}(t_p)$, are represented with colored dots—in the case of LCR—for a rebar diameter of 10 mm and 26 mm, respectively. It can be observed that as the diameter of the rebar decreases, the propagation period required to achieve brittle rupture at the elastic stage also decreases. This observation will be of great importance in Section 5 for the use of S&T models for the capacity assessment of corroded dapped-end beams. The tensile resistance of the corroded bar is calculated by multiplying the stress by the area of the uncorroded bar, A_0. The ultimate tensile strength, $F_{su,corr}(t_p)$, is calculated in Figure 18a for LCR ($I_{corr} = 0.5$ μA/cm^2), and in Figure 18b for MCR ($I_{corr} = 2.5$ μA/cm^2). Figure 18 shows the ultimate tensile strength, $F_{su,corr}(t_p)$, of the corroded rebars obtained by multiplying the ultimate strength of the corroded reinforcement, $f_{su,corr}(t_p)$, by the area of the uncorroded bar. The dotted lines indicate brittle failure in the elastic stage (i.e., before yielding).

Table 3 shows the calculated corroded values for bars with diameters 10, 12, and 14 mm, which will be used in Section 3.4 on the analytical method. It can be observed that, for the MCR case with higher corrosion rates ($t_p = 125$ years), the bars with minimum diameter (10 mm) have zero tensile strength due to the total loss of transversal cross-section.

Figure 18 shows that the tensile resistance of small diameter bars, such as the ties, is strongly affected by corrosive phenomena. Therefore, not only is the resistance

17517648, 2024, 2, Downloaded from https://onlinelibrary.wiley.com/doi/10.1002/suco.202301020 by University Degli Studi Di Parma Settore Biblioteche, Wiley Online Library on [15/05/2024]. See the Terms and Conditions (https://onlinelibrary.wiley.com/terms-and-conditions) on Wiley Online Library for rules of use; OA articles are governed by the applicable Creative Commons License

TABLE 3 Mechanical properties of corroded reinforcing steel for bars with 10, 12, and 14-mm diameters.

	LCR				MCR			
Bars	t_p [years]	$f_{sy,corr}$ [N/mm^2]	$f_{su,corr}$ [N/mm^2]	$\varepsilon_{su,corr}$ [%]	t_p [years]	$f_{sy,corr}$ [N/mm^2]	$f_{su,corr}$ [N/mm^2]	$\varepsilon_{su,corr}$ [%]
Ø10	25	526.50	599.09	5.66	20	361.36	361.36	0.17
	50	526.50	531.82	0.65	25	247.03	247.03	0.12
	75	432.12	432.12	0.21	30	133.10	133.10	0.06
	100	311.29	311.29	0.15	35	36.27	36.27	0.02
	125	182.81	182.81	0.09	40	0.00	0.00	0.00
Ø12	25	530.2	610.80	10.33	20	435.24	435.24	0.21
	50	530.2	562.39	4.28	25	345.27	345.27	0.16
	75	488.85	488.85	0.23	30	248.81	248.81	0.12
	100	396.42	396.42	0.19	35	152.55	152.55	0.07
	125	292.09	292.09	0.14	40	65.60	65.60	0.03
Ø14	25	507.7	614.63	8.51	20	481.04	481.04	0.23
	50	507.7	578.41	5.71	25	410.07	410.07	0.20
	75	507.7	522.48	1.38	30	331.38	331.38	0.16
	100	450.66	450.66	0.21	35	248.53	248.53	0.12
	125	367.09	367.09	0.17	40	165.80	165.80	0.08

Abbreviations: LCR, low corrosion rate; MCR, medium corrosion rate.

of corroded dapped-end beams less than that of uncorroded beams, but also a ductile-to-brittle failure mode transition can be observed, where the failure mode is attributed to the rupture of the bars in the elastic stage.

3.2.3 | Bond-slip behavior

The bond stress versus slip law for corroded bars is defined using Castel et al. model,[64] which is based on Model Code 2010 model[51] and on a damage parameter, D_c, that depends on the pit depth. The damage parameter, $D_c(t_p)$, is calculated as a function of the cross-sectional area of a pit, $A_p(t_p)$, as given by Equation (21):

$$D_c(t_p) = \begin{cases} 0 & A_p(t_p) < \Delta A_{s0} \\ \frac{2}{\alpha_b} s_t \log\left(1 + 0.25\left(A_p(t_p) - \Delta A_{s0}\right)\right) & A_p(t_p) \geq \Delta A_{s0} \end{cases} \quad (21)$$

where ΔA_{s0} is computed according to Equation (22):

$$\Delta A_{s0} = A_0 \left[1 - \left[1 - \frac{\alpha_b}{D_0}\left(7.53 - 9.32\frac{a}{D_0}\right)10^{-3}\right]^2\right], \quad (22)$$

where A_0 is the area of uncorroded bar, $\alpha_b = 6$ is a parameter that takes into account the type of corrosion, D_0 is the diameter of the uncorroded bar, and $a = 20$ mm is the concrete cover. The parameter s_t takes in to account the effect of stirrups. In the present case, the spacing of stirrups at dapped-ends is wide, therefore s_t is assumed to be 1. The value of the damage parameter, $D_c(t_p)$, allows to compute the ultimate bond stress, $\tau_{bu}(t_p)$, of the corroded bars according to,[65] as given by Equation (23):

$$\tau_{bu,corr}(t_p) = \left(1 - D_c(t_p)\right)\tau_{bu}, \quad (23)$$

where τ_{bu} is the ultimate bond stress for the uncorroded bar, reported in Figure 7. The resulting bond stress versus slip curves are plotted in Figure 19a and Figure 19b for a bar having diameter equal to 10 mm and for different values of the propagation time, t_p, respectively for low and medium corrosion rates.

Figure 19 shows that the bond strength can be severely affected by corrosive phenomena, leading to anchorage failure. Therefore, not only will the resistance of corroded dapped-end beams be lower than that of uncorroded ones, but also the failure mode may change from a ductile failure due to reinforcing steel yielding to brittle failure due to anchorage failure.

3.3 | Results of the NLFEA for the corrosion scenarios

Figure 20 shows the load versus vertical displacement D1 curves resulting from the NLFE analysis for corrosion

17517648, 2024, 2, Downloaded from https://onlinelibrary.wiley.com/doi/10.1002/suco.202301020 by University Degli Studi Di Parma Settore Biblioteche, Wiley Online Library on [15/05/2024]. See the Terms and Conditions (https://onlinelibrary.wiley.com/terms-and-conditions) on Wiley Online Library for rules of use; OA articles are governed by the applicable Creative Commons License

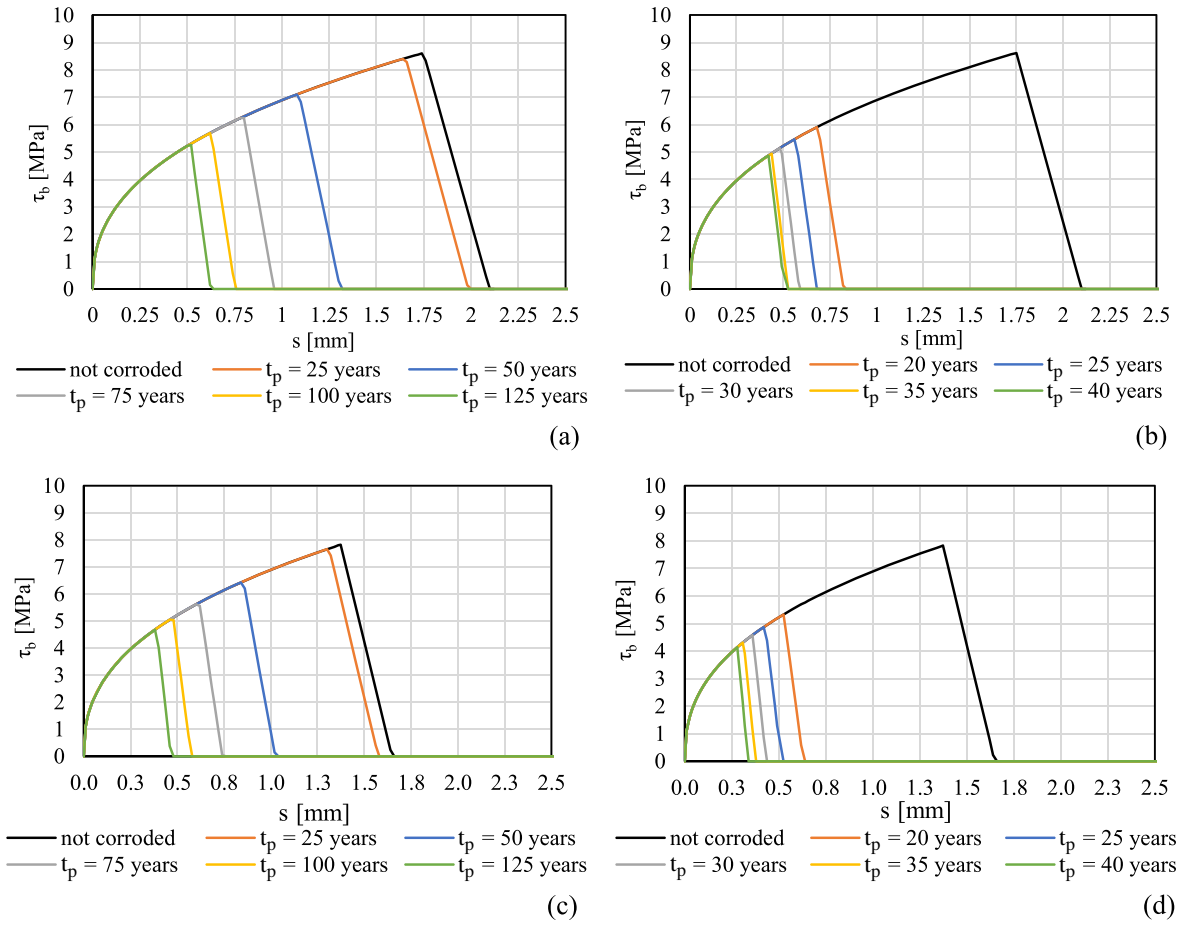

FIGURE 19 Bond stress versus slip curves plotted for different values of propagation time, t_p, for bars of diameter $\Phi = 10$ mm in the case of (a) LCR and (b) MCR and for bars of diameter $\Phi = 12$ mm in the case of (c) LCR and (d) MCR. LCR, low corrosion rate; MCR, medium corrosion rate.

Scenarios 1 and 2. In particular, the response of the corroded dapped-end beam for corrosion Scenario 1 is evaluated in Figure 20a and Figure 20c for low and medium corrosion rates, respectively. The response of the corroded dapped-end beam for corrosion Scenario 2 is shown in Figure 20b and Figure 20d for low and medium corrosion rates respectively. In case of MCR, after a period of 30 years, the high level of corrosion in the bars causes the beam to fail under its own weight. Figure 20 shows a large reduction in ductility for the corroded dapped-ends. This reduction in ductility is more pronounced for corrosion Scenario 1 than for corrosion Scenario 2. In fact, the ultimate displacement in corrosion Scenario 1 at the propagation time $t_p = 25$ years results equal to 32.4% of the ultimate displacement of the uncorroded dapped-ends, whereas in corrosion Scenario 2 it is equal to 71.2%.

Figure 21a and Figure 21b show the behavior of the corroded dapped-end beams over the propagation time for slow and medium corrosion rates respectively. The comparisons between the resistance of the corroded dapped-end beam for different propagation times registered for corrosion Scenarios 1 and 2, (Figure 21a and Figure 21b), are extremely interesting because they show that the reduction in capacity does not dependent on the extension of the zone affected by corrosion at the dapped-end, but it depends principally on the evolution of corrosion over time. Indeed, by considering the corresponding S&T model, the localized damage of a single tie can compromise the entire resisting mechanism.

Therefore, from a practical point of view, the results of NLFE analysis demonstrate that special care must be taken when inspecting the dapped-ends. In-situ inspection of existing dapped-ends must be carried out carefully to detect even small areas affected by corrosion. As evidenced in Figure 17 and Figure 18, the bars with smaller diameter values, such as stirrups, are more susceptible to brittle failure induced by corrosion and must be carefully analyzed during in situ inspection.

Figure 21 also shows that the residual life can be very different depending on the corrosion rate. Therefore, damage detection during in-situ inspection must

17517648, 2024, 2, Downloaded from https://onlinelibrary.wiley.com/doi/10.1002/suco.202301020 by University Degli Studi Di Parma Settore Biblioteche, Wiley Online Library on [15/05/2024]. See the Terms and Conditions (https://onlinelibrary.wiley.com/terms-and-conditions) on Wiley Online Library for rules of use; OA articles are governed by the applicable Creative Commons License

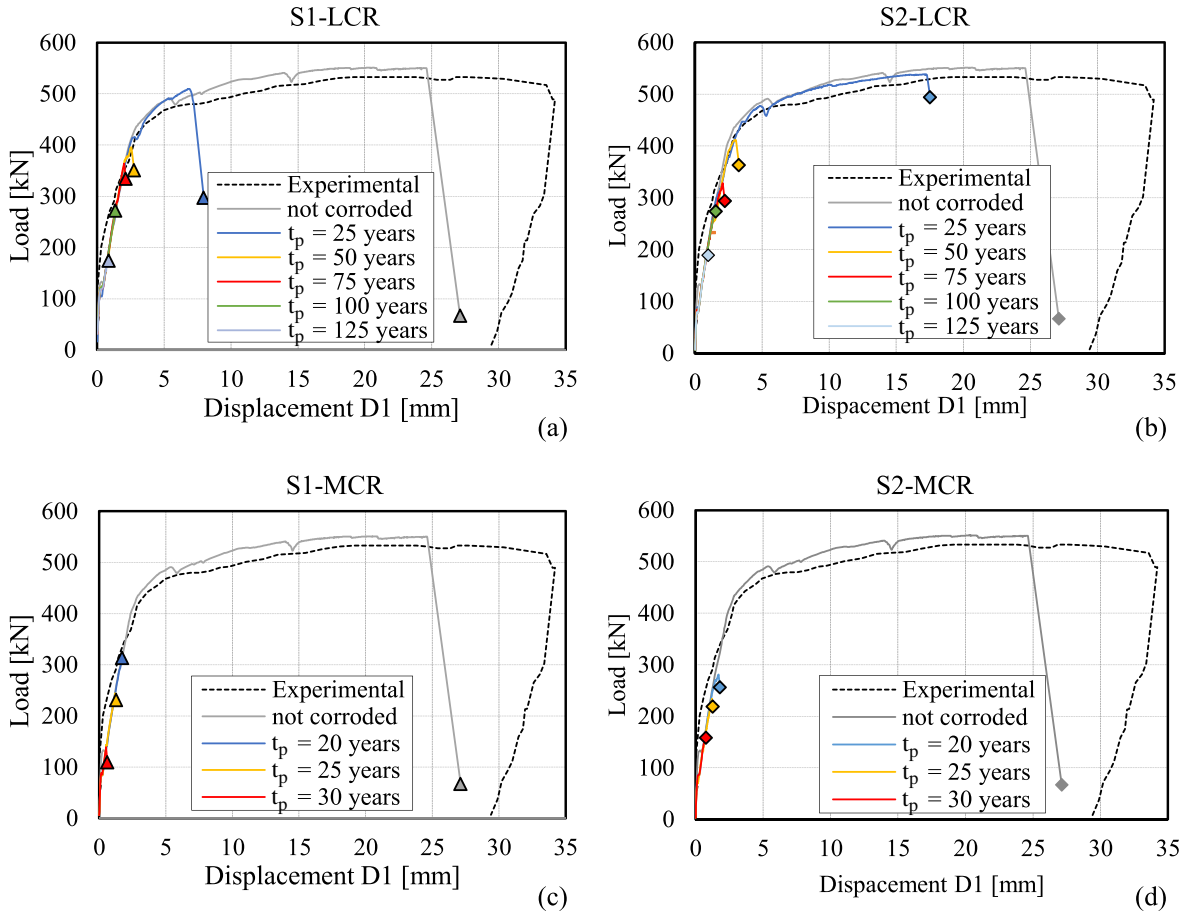

FIGURE 20 Load–displacement curve (D1) for the different corroded scenarios: (a) Scenario 1 and low corrosion rate, (b) Scenario 2 and low corrosion rate, (c) Scenario 1 and medium corrosion rate, and (d) Scenario 2 and medium corrosion rate.

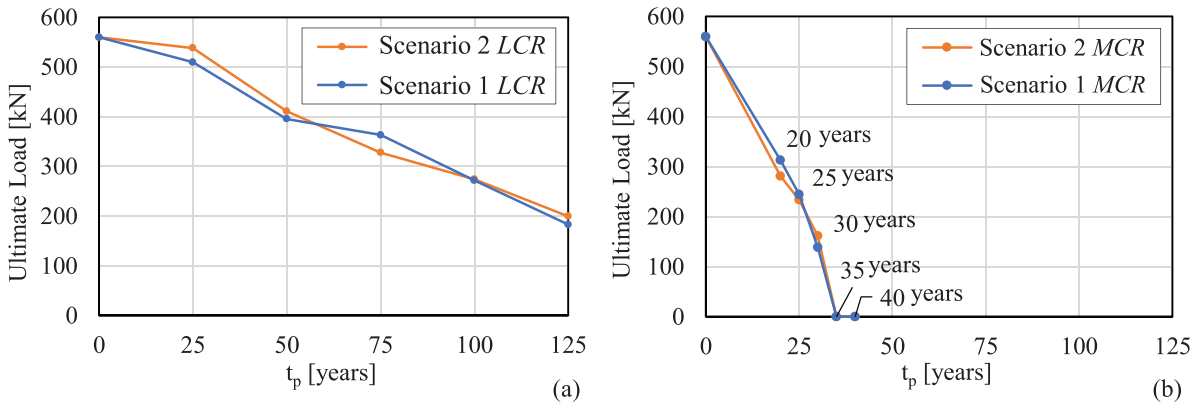

FIGURE 21 Resistance of the corroded dapped-end beam over the propagation time of (a) LCR and (b) MCR. LCR, low corrosion rate; MCR, medium corrosion rate.

always be correlated with the measurement of the velocity of the ongoing process to safely plan the frequency of inspections and/or to define the priority of repair or reinforcement interventions.

Table 4 and Table 5 show the sequence of yielding of the reinforcements for LCR and MCR respectively and different corrosion times t_p. In all cases, the failure of the dapped-end beam is attributed to the rupture of the vertical stirrups, but as the corrosion propagation time increases, the number of bars in the plastic stage decreases, leading to brittle failure.

In Table 4 and Table 5, the symbol "–" indicates that yielding is not reached and that the rupture of the rebars occurs in the elastic stage.

17517648, 2024, 2, Downloaded from https://onlinelibrary.wiley.com/doi/10.1002/suco.202301020 by University Degli Studi Di Parma Settore Biblioteche, Wiley Online Library on [15/05/2024]. See the Terms and Conditions (https://onlinelibrary.wiley.com/terms-and-conditions) on Wiley Online Library for rules of use; OA articles are governed by the applicable Creative Commons License

TABLE 4 Sequence of yielding in reinforcement for LCR in Scenarios 1 and 2.

	Sequence of yielding of reinforcement					Failure
Time t_p [years]	1	2	3	4	5	
0	Diagonal bar (Ø 14)	Stirrup 1 (Ø 10)	U-bar (Ø 12)	Stirrup 2 (Ø 10)	Stirrup 3 (Ø 10)	Stirrup 1 (Ø 10)
25	Diagonal bar (Ø 14)	Stirrup 1 (Ø 10)	U-bar (Ø 12)	Stirrup 2 (Ø 10)	Stirrup 3 (Ø 10)	Stirrup 1 (Ø 10)
50	Diagonal bar (Ø 14)	Stirrup 1 (Ø 10)	–	–	–	Stirrup 1 (Ø 10)
75	–	–	–	–	–	Stirrup 1 (Ø 10)
100	–	–	–	–	–	Stirrup 1 (Ø 10)
125	–	–	–	–	–	Stirrup 1 (Ø 10)

Abbreviation: LCR, low corrosion rate.

TABLE 5 Sequence of yielding in reinforcement for MCR in Scenarios 1 and 2.

	Sequence of yielding of reinforcement					Failure
Time t_p [years]	1	2	3	4	5	
0	Diagonal bar (Ø 14)	Stirrup 1 (Ø 10)	U-bar (Ø 12)	Stirrup 2 (Ø 10)	Stirrup 3 (Ø 10)	Stirrup 1 (Ø 10)
20	Diagonal bar (Ø 14)	Stirrup 1 (Ø 10)	U-bar (Ø 12)	Stirrup 2 (Ø 10)	Stirrup 3 (Ø 10)	Stirrup 1 (Ø 10)
25	Diagonal bar (Ø 14)	Stirrup 1 (Ø 10)	–	–	–	Stirrup 1 (Ø 10)
30	–	–	–	–	–	Stirrup 1 (Ø 10)

Abbreviation: MCR, medium corrosion rate.

The same concept is shown in Figure 22 where the strains of the bars are plotted for the uncorroded case (Figure 22a) and for Scenario 2 (global corrosion) for several time of propagation (Figure 22b–f). In these graphs it can be observed that the strain of corroded rebars is significantly reduced compared to the uncorroded ones, and that some bars do not reach the plastic stage when the failure of the first stirrup occurs (the dotted lines represent the yielding strain for each bar). Figure 22b,c shows that for propagation periods of less than 75 years, stirrups 1 can reach the hardening phase, therefore the diagonal bar, the U-bar, and the stirrup 2 can reach strain values equal to or higher than the ultimate strain of stirrup 1—which, being the reinforcement with the lowest value of the diameter, is the one characterized by the highest section loss and lowest value of ultimate strain.

Figure 22d–f shows that for propagation periods equal to and greater than 75 years, stirrup 1 remains in the elastic stage, the diagonal bar and the U-bar can reach strain values equal to or greater than the ultimate strain of stirrup 1, while stirrup 2 is characterized by lower strain values than stirrup 1. This observation will be useful in Section 5 for S&T models for the capacity assessment of corroded dapped-end beams.

Anchorage failures are also not recorded for the corroded dapped-end beams, as the bond stresses are always lower than the reduced bond strength of the corroded U-bars. Of course, the check of anchorage failure depends on reinforcement detailing and it is not possible to generate that ties rupture always anticipates anchorage failure. In fact, different detailing, such as bar location and anchorage length or different corrosion scenarios than those analyzed here, could lead to different results and failure modes than those obtained for this case study.

3.4 | S&CT method for corroded dapped-end beam

It is well known that S&T methods can be used if the ties forming the truss have sufficient ductility. In the case of corrosion, particular care must be taken as some of the rebars may break before yielding of all the ties forming the truss models has been achieved. If the concrete struts can resist to the applied forces in the uncorroded state, it could be assumed that the resistance of concrete struts is less critical during corrosion than the resistance of the ties. Therefore, in this section the S&T method has been applied without calculating of the resistance of nodes and concrete struts. In general, the resistance of concrete struts and nodes must be always checked for safety reasons since corrosion may cause splitting cracks and cover spalling.

A simplified S&T method—called S&CT method—is proposed here to evaluate the load-bearing capacity of corroded dapped-end beams, based on the following assumptions:

17517648, 2024, 2, Downloaded from https://onlinelibrary.wiley.com/doi/10.1002/suco.202301020 by University Degli Studi Di Parma Settore Biblioteche, Wiley Online Library on [15/05/2024]. See the Terms and Conditions (https://onlinelibrary.wiley.com/terms-and-conditions) on Wiley Online Library for rules of use; OA articles are governed by the applicable Creative Commons License

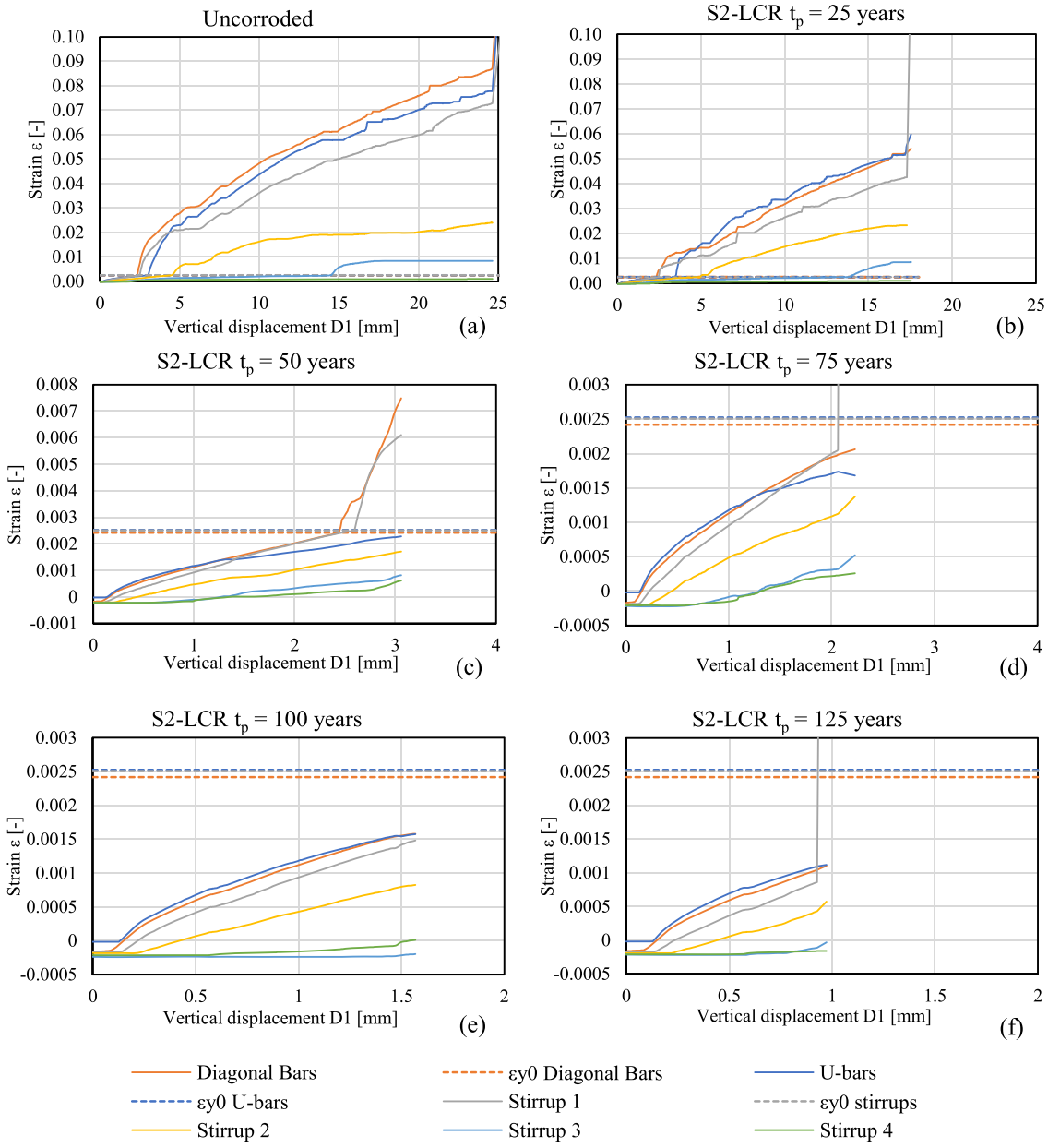

FIGURE 22 Strain of the bars for (a) uncorroded scenario and global corrosion (Scenario 2) for $t_p = 25$ years (b), $t_p = 50$ years (c), $t_p = 75$ years (d), $t_p = 100$ years (e), and $t_p = 125$ years (f).

- The critical tie is identified. It corresponds to the tie with the lowest diameter value, the highest section loss value, and the lowest ultimate strain value. The critical tie usually corresponds to stirrups, which are characterized by the lowest concrete cover and the lowest initiation period.
- The stress–strain of the critical tie is evaluated as a function of the section loss, according to the model proposed by Chen et al.[15]
- The same damage evolution is conservatively assigned to all ties forming the truss, even if they are characterized by higher concrete cover. Then, the stress–strain relationship of the critical tie, calculated at point (2), is assigned to all the ties forming the S&T model.
- If the stirrup 1 can reach the hardening phase, the strain values of all the rebars (stirrups near the nib zone and rebars) are assumed equal to the ultimate strain of the critical tie. Thus, in this case, the contributions of the other stirrups near the nib are considered. If the stirrup 1 remains in the elastic stage, the resistance is conservatively evaluated by considering only the contribution of stirrup 1 and by neglecting the resisting contributions of the other stirrups, characterized by strain values lower than the yielding strain

17517648, 2024, 2, Downloaded from https://onlinelibrary.wiley.com/doi/10.1002/suco.202301020 by University Degli Studi Di Parma Settore Biblioteche, Wiley Online Library on [15/05/2024]. See the Terms and Conditions (https://onlinelibrary.wiley.com/terms-and-conditions) on Wiley Online Library for rules of use; OA articles are governed by the applicable Creative Commons License

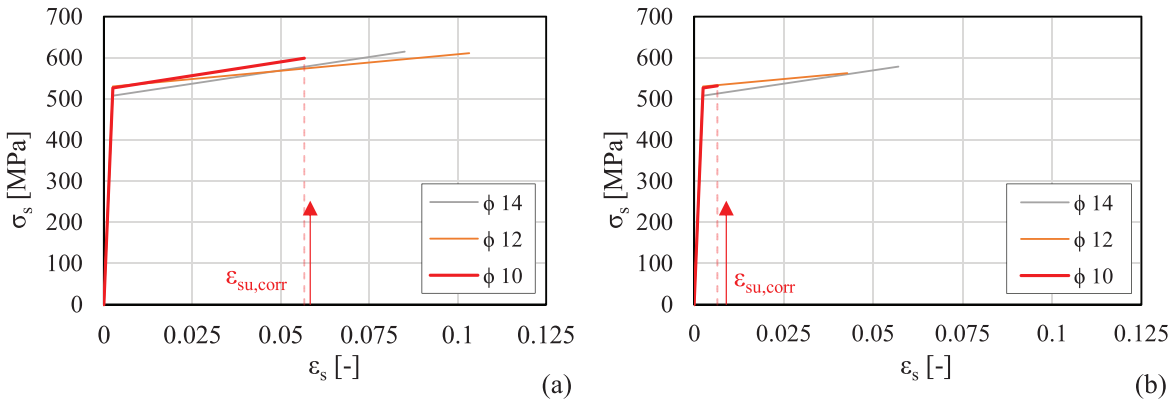

FIGURE 23 Stress–strain bilinear curve for corroded rebars for (a) $t_p = 25$ years and (b) $t_p = 50$ years.

value. Furthermore, in this latter case, the ultimate strain value of the rebars is assumed equal to the ultimate strain of stirrup 1.

- The reduced tensile yielding and ultimate strengths of the critical tie are calculated and assigned to all ties forming the truss.
- The tensile resistance of all the ties forming the truss is calculated by multiplying the reduced tensile strength of the critical tie by the uncorroded transversal cross-section area of each tie.

Figure 23 shows that, since the stirrups are the critical tie with the smallest diameter, the other reinforcements certainly have a higher ductility. In fact, Figure 23a and Figure 23b, for two different propagation periods ($t_p = 25$ years and 50 years) show that the other ties—with diameters equal to 12 and 14 mm—have a ductility higher than the critical tie—with a diameter equal to 10 mm.

As shown in the above section, the number of stirrups considered in the *S&T* method to evaluate the ultimate load of the dapped-end beams is very relevant. The presented S&CT method is applied to Scenario 2 (global corrosion) with low corrosion rate. In this case, different numbers of stirrups are considered over time because of the relevant distance between them. In the first case ($t_p = 25$ years) the first two stirrups are considered in the calculation of the model A, while in the other cases (from $t_p = 50$ to $t_p = 125$ years) only one stirrup is considered to evaluate the ultimate load in the model A due to the fact that the failure of the stirrups occurs almost in elastic stage (Figure 17a) and the second stirrup, which has a strain smaller than stirrup 1, will remain in elastic stage.

The resistance of the analyzed dapped-ends beam obtained by NLFE analyses, and the presented S&CT method are shown in Figure 24—in blue and green, respectively—as a function of different period of propagation t_p. To compare the results of NLFEA obtained by using the stress–strain relationship for reinforcement up to the ultimate strain value, the resistance obtained by the *S&T* method is calculated by assuming the ultimate strength of the critical tie for all the reinforcement. Both NLFE and S&CT based methods can predict the reduction in resistance due to corrosion.

Similarly to the case of uncorroded dapped-ends beam, the resistance obtained by NLFE analysis results higher than that obtained by the S&CT based method. To highlight the fundamental role played by chloride-induced corrosion in the reduction ductility, Figure 24 also shows in gray the resistance obtained by S&CT method by reducing only the cross-section of the ties without reducing the ultimate strain. The resistances obtained by this latter approach are unconservative and in some cases even higher than those obtained by NLFE analyses. To consider an assessment situation in the engineering practice, Figure 24 shows in yellow the results of the S&CT method obtained by assuming the yield strength or the strength at the elastic stage, depending on the level of corrosion. The yellow bars show that, the resistances obtained by the S&CT method, are lower than those obtained by NLFEA and that the ratio between the NLFEA resistance and the S&CT resistance remains almost constant for all the propagation periods. Finally, NLFEA can be a suitable tool to study the sequence of events occurring in uncorroded and corroded dapped-ends, allowing to understand the change in the expected mechanisms and failure mode. Furthermore, these models are developed in a deterministic way, taking into account the average properties of the materials. In a possible assessment situation, model uncertainties need to be considered, using appropriate safety factors, especially in the case of corrosion, where further studies need to be developed.

17517648, 2024, 2, Downloaded from https://onlinelibrary.wiley.com/doi/10.1002/suco.202301020 by University Degli Studi Di Parma Settore Biblioteche, Wiley Online Library on [15/05/2024]. See the Terms and Conditions (https://onlinelibrary.wiley.com/terms-and-conditions) on Wiley Online Library for rules of use; OA articles are governed by the applicable Creative Commons License

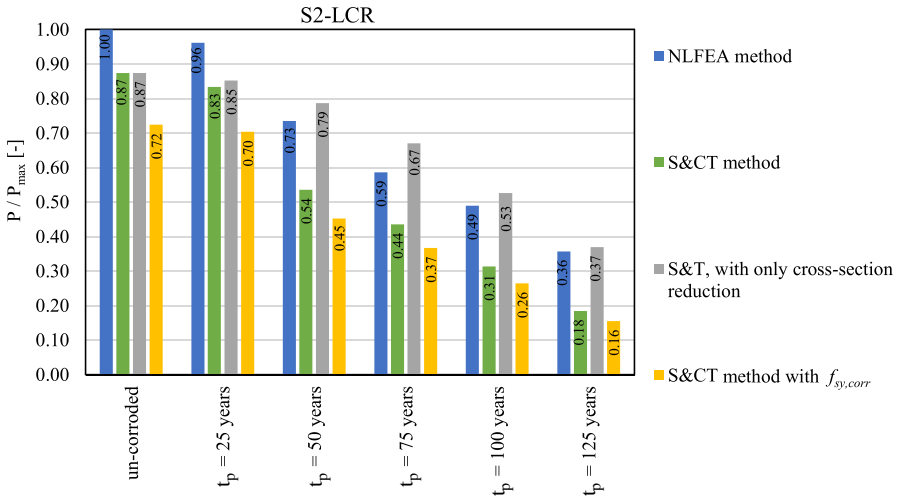

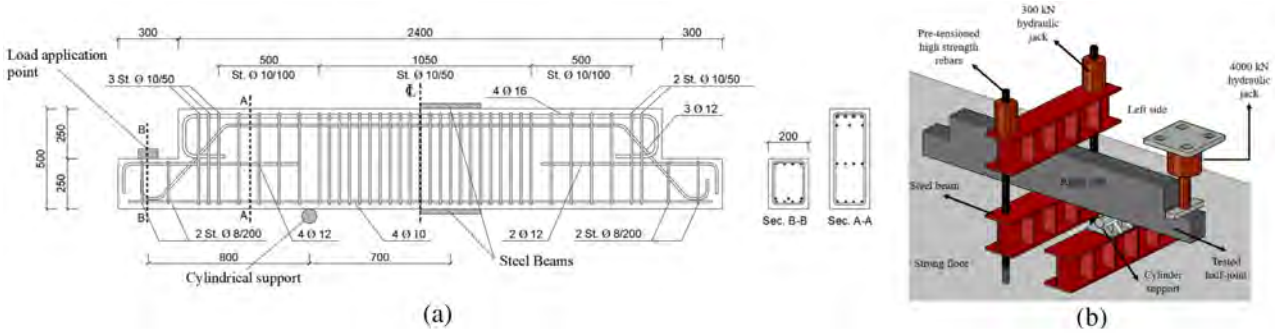

FIGURE 24 Results of numerical and analytical S&T methods without and with corrosion. S&T, strut-and-tie.

FIGURE 25 (a) Reinforcements of the dapped-end beam. Dimensions in mm. (b) Test set-up (after Reference 49).

4 | CASE STUDY 2: ARTIFICIALLY CORRODED DAPPED-END BEAM

4.1 | Geometry, instrumentation layout, and mechanical properties of concrete and reinforcing steel

In this section, the validations of the finite element model and the S&CT model previously described are presented. As reference case, the very recent experimental tests conducted on uncorroded and corroded dapped-end beams by Di Carlo et al.[49] are used. In this experimental campaign, several dapped-end beams were experimentally tested and, in the present work, the specimens G2-NC (uncorroded) and G2-C (corroded) are selected. Numerical results of other specimens are reported in the work of the authors.[66] In the corroded specimens G2-C, the spatial distribution of the corrosion was measured; in particular, the pit-depth along stirrups, diagonal bars, and horizontal bars was available (rebars highlighted in red in Figure 26). The geometry and reinforcement layout are shown in Figure 25a, while the mechanical properties of concrete and uncorroded steel rebars are reported in Table 6 and Table 7 respectively.

The test setup, shown in Figure 25b, was designed to simulate the structural continuity of an existing dapped-end beam. During the test, the specimen was anchored to the laboratory strong floor by means of two steel beams and two pretensioned high strength rebars.

A cylindrical support was positioned at 700 mm from the axis of the steel beams while the load was applied at the nib at a distance equal to 1500 mm from the axis of the steel beams (Figure 25a). For further details about the experimental tests and corrosion process see Reference 49.

4.2 | Finite element modeling of the uncorroded and corroded dapped-end beams

For the finite element model, the same procedure described in Section 2 is used. To reduce the computational cost, only the loaded part of the dapped-end beam was modeled. Also in this case, the bars and stirrups were

17517648, 2024, 2, Downloaded from https://onlinelibrary.wiley.com/doi/10.1002/suco.202301020 by University Degli Studi Di Parma Settore Biblioteche, Wiley Online Library on [15/05/2024]. See the Terms and Conditions (https://onlinelibrary.wiley.com/terms-and-conditions) on Wiley Online Library for rules of use; OA articles are governed by the applicable Creative Commons License

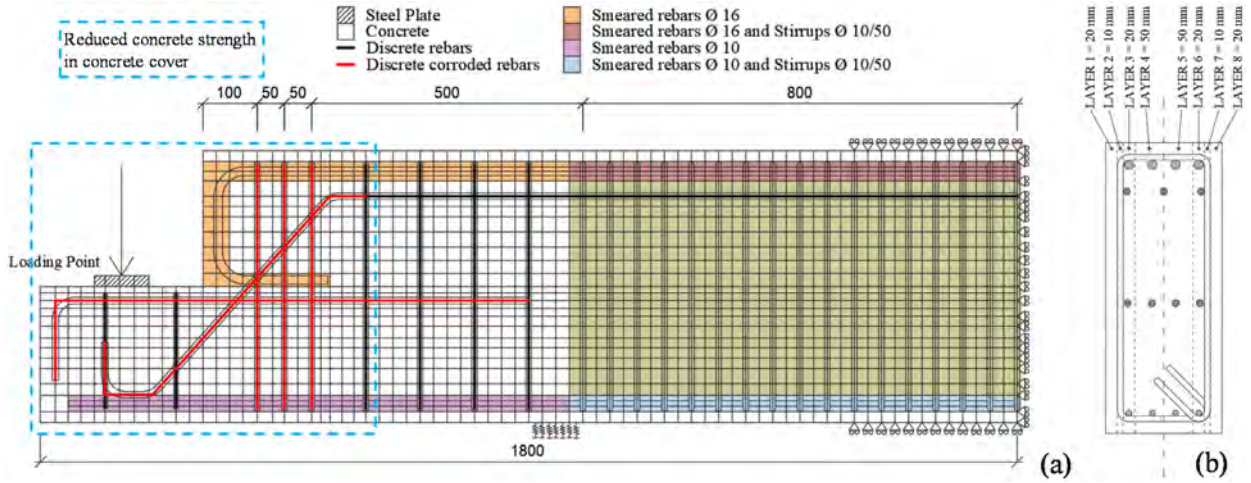

FIGURE 26 (a) Finite element mesh of the dapped-end beam. (b) Position of reinforcements and layers in section. Dimensions in mm.

TABLE 6 Mechanical properties of concrete.

Property	Value	Unit
f_{cm}	43.66	N/mm^2
f_{ctm}	2.88	N/mm^2
E_{cm}	35,139	N/mm^2
ρ	2500.00	kg/m^3
ν	0.20	–
G_F	0.102	N/mm
G_C	25.47	N/mm

modeled with both smeared and discrete approaches. For the rebars modeled with discrete approach, the slip of the reinforcement was considered. The mesh of the model, the boundary conditions, and the type of steel modeling are resumed in Figure 26. The loading steel plate was modeled using the same concepts described in Section 2.2.2, while in the zone of the support, springs with elevated stiffness ($K = 10^6$ N/mm) to prevent stress localizations were used. To simulate the presence of the steel beams in the left part of the beam, both vertical displacements on top and bottom of the beam and horizontal displacements along the beam section were blocked.

For the specimen subjected to corrosion, the constitutive laws of the corroded rebars (highlighted in red in Figure 26a) were modified in terms of ultimate strength and strain and in terms of bond-slip behavior. In particular, for each single corroded rebar, the mechanical properties were reduced as function of the maximum section loss μ measured along the bar itself and applied at the whole corroded rebar. The reduction of the compressive strength of the concrete cover was considered in the zones near the corroded stirrups (highlighted in blue in Figure 26a).

The same procedure described in Section 3.2 was used to define the reduced mechanical properties for concrete cover, reinforcing steel, and bond-slip behavior.[15,63,64] The numerical values for rebars and stirrups are reported in Table 8 for each single stirrup leg and bar. An average cross-section reduction of all the external rebars in the whole zone of cracking was considered and the compressive strength of cracked concrete cover was reduced from 43.65 to 16.35 N/mm^2.

4.3 | Results of NLFE analyses of corroded dapped-end beam

The results of the NLFEA are reported in Figure 27 for the uncorroded case (Figure 27a) and the corroded one (Figure 27b). The comparison with the experimental results is carried out in terms of load–displacement

TABLE 7 Mechanical properties of uncorroded reinforcing steel.

Diameter	$f_{sy,0}$ [N/mm^2]	$f_{su,0}$ [N/mm^2]	$\epsilon_{su,0}$ [%]	τ_{bu} [N/mm^2]	$s(\tau_{bu})$ [mm]
Ø10	516.00	615.00	11.6	8.95	0.389
Ø12	565.00	628.20	10.7	6.99–7.93[a]	0.210–0.288[a]
Ø16[b]	464.00	627.50	10.5	–	–

[a]There are different values for horizontal rebars and diagonal rebars, respectively.
[b]For rebars Ø16 perfect bond is considered.

17517648, 2024, 2, Downloaded from https://onlinelibrary.wiley.com/doi/10.1002/suco.202301020 by University Degli Studi Di Parma Settore Biblioteche, Wiley Online Library on [15/05/2024]. See the Terms and Conditions (https://onlinelibrary.wiley.com/terms-and-conditions) on Wiley Online Library for rules of use; OA articles are governed by the applicable Creative Commons License

TABLE 8 Mechanical properties of corroded reinforcing steel for bars with 10 and 12 mm diameters.

Corroded steel rebars							
		Position of legs and bars[a]	Maximum section loss, μ [−]	$f_{sy,corr}$ [N/mm^2]	$f_{su,corr}$ [N/mm^2]	$\varepsilon_{su,corr}$ [−]	$\tau_{bu,corr}$ [N/mm^2]
Ø10	Stirrup 1	Left	0.138	516	530	0.0076	7.49
		Right	0.289	437	437	0.0021	6.62
	Stirrup 2	Left	0.277	445	445	0.0022	6.67
		Right	0.095	516	556	0.0186	7.89
	Stirrup 3	Left	0.197	493	493	0.0025	7.07
		Right	0.027	516	598	0.0483	8.95
Ø12	Diagonal rebars	Left	0.105	565	582	0.0284	6.56
		Middle	0.019	565	639	0.0627	7.93
		Right	0.052	565	617	0.0640	7.25
	Horizontal rebars	Left	0.494	329	329	0.0016	4.30
		Central	0.062	565	611	0.0411	6.24
		Central	0.079	565	599	0.0355	6.03
		Right	0.126	565	569	0.0233	5.61

[a]For the position of stirrup legs and rebars refer to Figure 26a.

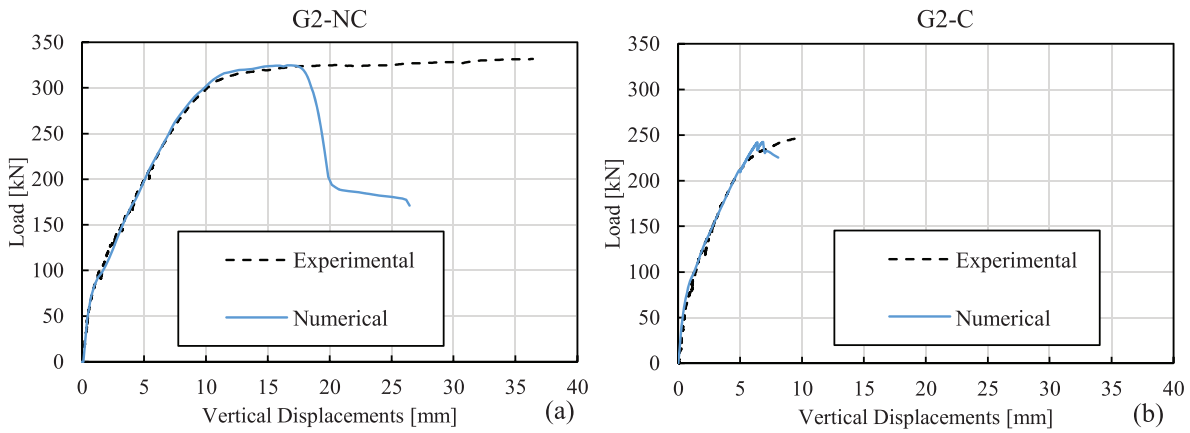

FIGURE 27 Comparison between experimental and NLFEA results: (a) uncorroded case G2-NC and (b) corroded case G2-C. NLFEA, nonlinear finite element analyses.

curves (the curves have been truncated at maximum load). In the graph it is possible to see that the numerical model can predict the maximum load. The crack patterns at ultimate load from the NLFEA are in good agreement with the experimental tests (Figure 28). In addition, the model can reproduce the failure mechanism of the experimental tests: (i) for the uncorroded case (G2-NC) the failure is governed by the collapse of the compression strut that reaches the roller at the bottom part of the dapped-end beam and (ii) for the corroded case (G2-C) the failure is governed by the rupture of the corroded stirrups near the nib. The numerical model shows that, when the ultimate load is reached in both cases (G2-NC and G2-C), the maximum bond stress values are attained in the horizontal and diagonal bars near the re-entrant corner; such high values are attributed to the high crack width observed in this area. Even though in some areas of the cracked zone near the nib, maximum bond stresses were reached, no anchorage failure was detected thanks to the sufficient length of anchorage of the diagonal and horizontal rebars.

17517648, 2024, 2, Downloaded from https://onlinelibrary.wiley.com/doi/10.1002/suco.202301020 by University Degli Studi Di Parma Settore Biblioteche, Wiley Online Library on [15/05/2024]. See the Terms and Conditions (https://onlinelibrary.wiley.com/terms-and-conditions) on Wiley Online Library for rules of use; OA articles are governed by the applicable Creative Commons License

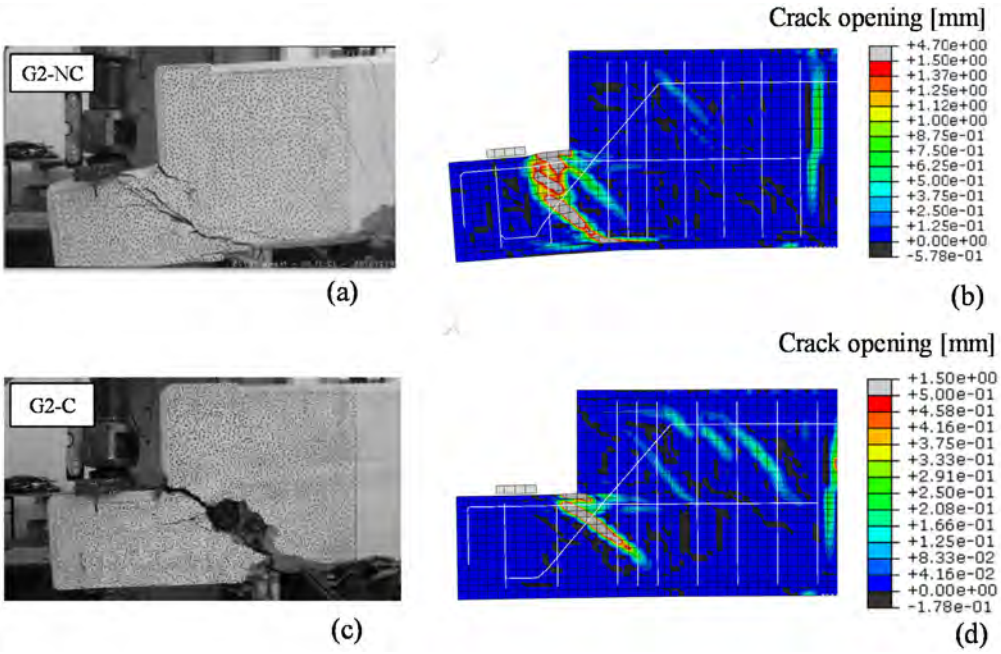

FIGURE 28 Comparison between experimental[49] and NLFEA crack patterns at failure: (a) experimental and (b) numerical crack pattern for the test G2-NC; (c) experimental and (d) numerical crack pattern for the test G2-C. NLFEA, nonlinear finite element analyses.

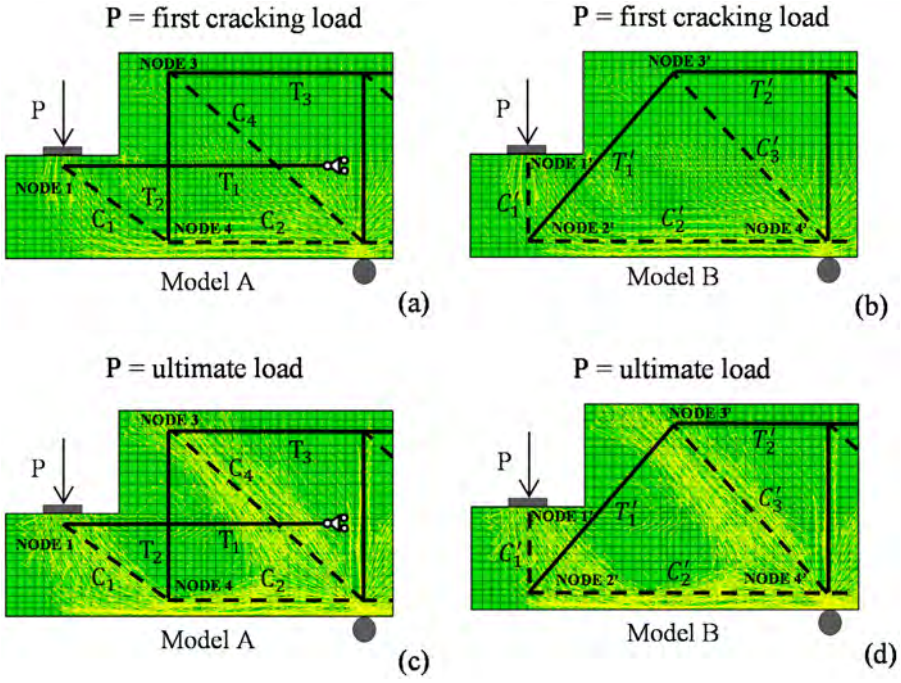

FIGURE 29 Comparison of NLFEA minimum principal stress field and strut-and-tie models A and B at first cracking load (a and b) and ultimate load (c and d).

4.4 | S&T method for uncorroded and corroded dapped-end beam

The S&T analytical models were used also for this case. To calculate the ultimate load capacity (P_{ult}) for the uncorroded and corroded cases, the same procedure and assumptions described in Sections 2.4 and 3.4 were adopted. Also in this case, for the analytic calculations two truss-models A and B were used, and Figure 29 shows the minimum principal stress at first cracking load and at the ultimate load. It is possible to verify the correspondence of the truss position and inclination with the NLFEA principal stresses for both models A and B.

The ultimate load for the model A and model B was evaluated according to Equations (1) and (5), respectively, without using the coefficient 3/2 because of the different structural scheme. Then, the total ultimate load was evaluated. It is worth to note that, for the ultimate

17517648, 2024, 2, Downloaded from https://onlinelibrary.wiley.com/doi/10.1002/suco.202301020 by University Degli Studi Di Parma Settore Biblioteche, Wiley Online Library on [15/05/2024]. See the Terms and Conditions (https://onlinelibrary.wiley.com/terms-and-conditions) on Wiley Online Library for rules of use; OA articles are governed by the applicable Creative Commons License

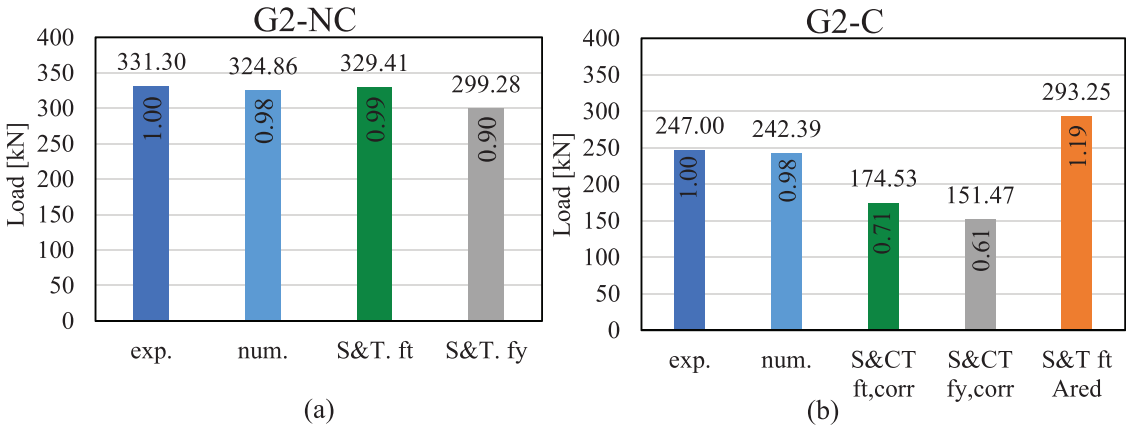

FIGURE 30 Results of numerical and analytical S&T methods (a) without and (b) with corrosion. S&T, strut-and-tie.

load capacity of Model A, the first three stirrups near the nib were considered with tie T_2; in this case, they were considered as one single tie since their distance is relatively short with respect to the other stirrups. The results of the analytic calculation are reported in Figure 30 by considering both yielding and ultimate strength for the uncorroded case (Figure 30a) and reduced yield and ultimate strength for the corroded case (Figure 30b). In the same figure, the ultimate loads are compared to numerical NLFEA and experimental results.

From the comparison between experimental and analytical results of the analyzed dapped-ends beam it is possible to observe that also in this case the S&T method provides conservative estimations of the ultimate load. The highest resistance can be obtained by S&T methods when ultimate strength, f_{st}, is used for the steel, while a more conservative value is obtained if the yielding strength, f_{sy}, is used. This confirms the recommendations of the main standards and guidelines on the use of yield strength when conducting safety checks of existing structures. Considering the S&CT method (Figure 30b), the ultimate load is underestimated by 29% and 39% using ultimate and yielding strength, respectively, which is in line with the results of the first case study. Figure 30b shows also the results obtained considering only the reduced cross-section of the corroded rebars without reduction in strength and strain. In this case, the S&T method applied to corroded Gerber saddles provided unconservative result (orange bar in the graph).

5 | CONCLUSIONS

In the present paper a procedure for NLFE modeling and a simple S&T based procedure for dapped-end beams subjected to chloride-induced corrosion are proposed. The principal effects of corrosion, such as reduction of strength and ductility of the bars, reduction of bond, and cracking of the concrete cover are considered in the modeling. The proposed method is applied to two of the most recent experimental tests in the literature. The procedure is firstly applied to a first case study[48] of an uncorroded dapped-end beam experimentally tested, then, two different corrosion scenarios are simulated and applied to the same case study. The second case study[49] is used to validate the model with the experimental outcomes of tests carried out on corroded dapped-end beams. From the results of the analyses, it can be seen that the effects of corrosion can change the failure mode of dapped-end beams with important consequences on resisting mechanisms, ultimate load, and ductility. However, considering the first case study, the reduction in ultimate load over time for both corrosion scenarios S1 and S2 is comparable; this means that the resistance of corroded dapped-end beams is not significantly affected by the extension of the corroded zone, but it principally depends on the corrosion rate. The results obtained from the second case study confirm that the model can help to predict ultimate load capacity in presence of chloride corrosion.

In the selected cases, no anchorage failures were detected. However, it has been observed that, when corrosion occurs, the bond stresses in the horizontal rebars, approach or even reach (for small parts near the cracks) the maximum bond stresses value τ_{bu}. Hence, a careful check of anchorage lengths must be carried out in existing dapped-end beams, because even though this is not the case, the designed anchorage lengths may not be sufficient in presence of corrosion.

The modeling of corrosion damage with NLFE analysis allows to predict the capacity reduction of corroded dapped-end beams over time, providing useful insights

17517648, 2024, 2, Downloaded from https://onlinelibrary.wiley.com/doi/10.1002/suco.202301020 by University Degli Studi Di Parma Settore Biblioteche, Wiley Online Library on [15/05/2024]. See the Terms and Conditions (https://onlinelibrary.wiley.com/terms-and-conditions) on Wiley Online Library for rules of use; OA articles are governed by the applicable Creative Commons License

for in situ inspections of corroded dapped-end beams, which could be implemented in guidelines for the risk assessment and/or maintenance of existing structures and infrastructures. However, the NLFE analyses are not always suitable tools for daily engineering practice but can be used to understand the failure mechanisms and to calibrate simplified methods. In this regards the S&CT method for the prediction of the resistance of corroded dapped-end beams was presented. This new method, which uses simply hypothesis on corroded ties, provides conservative results in terms of ultimate load compared to the numerical and experimental results for uncorroded dapped-end beams. On the contrary, it can lead to unsafe predictions if corrosion is introduced by only reducing the reinforcement area. For the analyzed case study, the presented S&CT method overcomes this problem, resulting in a useful tool to easily assess the resistance of corroded dapped-end beams.

The proposed novel NLFE and S&CT methodologies are promising tools that can be further validated when new experimental evidence becomes available. These tools can be used in research but also in engineering practice to plan inspection, preliminary assessment, monitoring, repairing, retrofit, or dismantlement of bridges.

ACKNOWLEDGMENTS

The study presented was carried out as part of the Agreement between "Superior Council of Public Works" and ReLUIS according to DM 578/2020 and DM 240/2022.

The authors would like to thank the University of Rome "Tor Vergata" in particular, Zila Rinaldi and Fabio Di Carlo for their support regarding the experimental data of the second case study.

CONFLICT OF INTEREST STATEMENT

The authors declare no conflicts of interest.

DATA AVAILABILITY STATEMENT

The data that support the findings of this study are available from the corresponding author upon reasonable request.

ORCID

Beatrice Belletti https://orcid.org/0000-0002-4382-9930

REFERENCES

1. McDaid E, Loh GS, Shave J, Pearson-Kirk D, Bennetts J, Valerio P. Half-joint, deck hinge and post-tensioned concrete bridges: risk management and assessment. Proc Inst Civ Eng Bridge Eng. 2021;174(3):205–18.
2. Desnerck P, Lees JM, Valerio P, Loudon N, Morley CT. Inspection of RC half-joint bridges in England: analysis of current practice. Proc Inst Civ Eng Bridge Eng. 2018;171(4):290–302.
3. Palmisano F, Asso R, Chiaia B, Marano GC, Pellegrino C. Structural assessment of existing R.C. half-joint bridges according to the new Italian guidelines. J Civ Struct Heal Monit. 2022;13:1–25.
4. Campione G, Granata MF, Papia M, Zizzo M. Degraded Gerber saddles in RC bridges. J Perform Constr Facil. 2023;37(2):88–100.
5. di Prisco M, Colombo M, Martinelli P, Coronelli D. The technical causes of the collapse of Annone overpass on SS. 36. In Il calcestruzzo strutturale oggi: teoria, impieghi, materiali, tecniche, pp. 1–16. ITA; 2018.
6. di Prisco M, Colombo M, Martinelli P. Structural aspects of the collapse of a RC half-joint bridge: case of the Annone overpass. J Bridg Eng. 2023;28(11):1–18.
7. Shakir QM. Reinforced concrete dapped end beams – state of the art. Int J Appl Sci. 2018;1(2):44–57.
8. Mattock AH, Chan TC. Design and behavior of dapped-end beams. PCI J. 1979;24(6):28–45.
9. Leonhardt F, Mönnig E. Vorlesungen über Massivbau: Teil 1: Grundlagen zur Bemessung im Stahlbetonbau. Vol 1. Berlin, Germany: Springer-Verlag; 2013.
10. Schlaich J, Schaefer K, Jennewein M. Toward a consistent design of structural concrete. PCI J. 1987;32(3):74–150.
11. EN 1992-1-1:2004. Eurocode 2: design of concrete structures – Part 1-1: general rules and rules for buildings. Brussels, Belgium: European Committee for Standardization; 2014.
12. ACI CODE 318-19 (22). Building code requirements for structural concrete and commentary (reapproved 2022). Farmington Hills, MI, UK: American Concrete Institute; 2019.
13. PCI. PCI design handbook: precast and prestressed concrete. 7th ed. Chicago, IL, USA: Prestressed Concrete Institute; 2014.
14. Desnerck P, Lees JM, Morley CT. Impact of the reinforcement layout on the load capacity of reinforced concrete half-joints. Eng Struct. 2016;127:227–39.
15. Chen E, Berrocal CG, Fernandez I, Löfgren I, Lundgren K. Assessment of the mechanical behaviour of reinforcement bars with localised pitting corrosion by digital image correlation. Eng Struct. 2020;219(May):110936.
16. Taher SE-DMF. Strengthening of critically designed girders with dapped ends. Proc Inst Civ Eng Struct Build. 2005;158(2):141–52.
17. Mitchell D, Cook WD, Peng T. Importance of reinforcement detailing. ACI Spec Publ. 2010;273:1–16.
18. Mohammed AAA. Nonlinear three-dimensional finite element analysis of reinforced concrete dapped-end beams. Iraqi J Civ Eng. 2010;9(1):1–16.
19. Hayder MA-J. Modelling of dapped-end beams using Abaqus software. Int J Civ Eng Technol. 2018;9(1):1–10.
20. Abdel-Moniem AEN, Madkour H, Abdullah A, Farah K. Numerical investigation of reinforced-concrete beams with half-joints. Proc Inst Civ Eng Struct Build. 2020;173(10):715–29.
21. Moreno JY, Meli R. Experimental study and numerical simulation of the behaviour of concrete dapped-end beams. Eng Model. 2013;26(1–4):15–25.
22. Aswin M, Mohammed BS, Liew MS, Syed ZI. Shear failure of RC dapped-end beams. Adv Mater Sci Eng. 2015;2015:1–11.
23. Hasa M, Zich M. Nonlinear analysis of precast dapped-end beams. Solid State Phenom. 2017;259:184–9.

17517648, 2024, 2, Downloaded from https://onlinelibrary.wiley.com/doi/10.1002/suco.202301020 by University Degli Studi Di Parma Settore Biblioteche, Wiley Online Library on [15/05/2024]. See the Terms and Conditions (https://onlinelibrary.wiley.com/terms-and-conditions) on Wiley Online Library for rules of use; OA articles are governed by the applicable Creative Commons License

24. Aksoylu C, Özkılıç YO, Arslan MH. Damages on prefabricated concrete dapped-end purlins due to snow loads and a novel reinforcement detail. Eng Struct. 2020;225:111225.
25. Don W, Suryanto B, Tambusay A, Suprobo P. Forensic assessments of the influence of reinforcement detailing in reinforced concrete half-joints: a nonlinear finite element study. Structure. 2022;38:689–703.
26. Aswin M, Mohammed B, Liew MS, Syed ZI. Prediction of RC beams failure load using non-linear finite element analysis. Int J Appl Eng Res. 2015;10(22):42974–80.
27. Abdel-Moniem A, Madkour H, Abdullah A, Farah K. Non-linear numerical analysis of pre-cast reinforced concrete dapped ends beams. Int Res J Eng Technol. 2018;5(10):1735–40.
28. Syed ZI, Hejah ES, Mohamed OA. Modelling of dapped-end beams under dynamic loading. Int J Mech Eng Robot Res. 2017;6(3):242–7.
29. Syed ZI, Kewalramani M, Hejah ES. Structural reliability of dapped end beams with different reinforcement layouts under dynamic loading. IOP Conf Ser Mater Sci Eng. 2019;575:012003.
30. Nagy-György T, Sas G, Dăescu AC, Barros JAO, Stoian V. Experimental and numerical assessment of the effectiveness of FRP-based strengthening configurations for dapped-end RC beams. Eng Struct. 2012;44:291–303.
31. Abdel-Moniem A, Madkour H, Farah K, Abdullah A. Numerical investigation for external strengthening of dapped-end beams. Int J Civ Environ Eng. 2018;12(10):1017–27.
32. Özkılıç YO, Aksoylu C, Arslan MH. Experimental and numerical investigations of steel fiber reinforced concrete dapped-end purlins. J Build Eng. 2021;36:102119.
33. Özkılıç YO, Yazman Ş, Aksoylu C, Arslan MH, Gemi L. Numerical investigation of the parameters influencing the behavior of dapped end prefabricated concrete purlins with and without CFRP strengthening. Constr Build Mater. 2021;275:122173.
34. Mihaylov B, Rajapakse C, Berger PH. Effect of steel fibers on the ultimate flexural behavior of dapped-end connections. Eng Struct. 2022;259(March):114147.
35. Santarsiero G, Masi A, Picciano V. Durability of Gerber saddles in RC bridges: analyses and applications (Musmeci bridge, Italy). Inf Dent. 2021;6(2):25.
36. Chijiwa N, Suryanto B, Kurihara R. Forensic analysis of reinforced concrete half-joints using nonlinear finite element analysis. Dent Tech. 2020;6(1):216–26.
37. Rosso MM, Asso R, Aloisio A, Di Benedetto M, Cucuzza R, Greco R. Corrosion effects on the capacity and ductility of concrete half-joint bridges. Constr Build Mater. 2022;360(July):129555.
38. Abeysinghe SA, Yapa HD. Numerical simulation of damaged RC half-joint beams: towards appraisal and retrofitting. Proc Inst Civ Eng Struct Build. 2023;176(11):921–37.
39. Granata MF, La Mendola L, Messina D, Recupero A. Assessment and strengthening of reinforced concrete bridges with half-joint deterioration. Struct Concr. 2023;24(1):269–87.
40. Spinella N, Messina D. Load-bearing capacity of Gerber saddles in existing bridge girders by different levels of numerical analysis. Struct Concr. 2022;24:211–26.
41. De Domenico D, Mazzeo M, Messina D, Recupero A. Safety assessment of corroded PC half-joint bridges through an advanced mechanochemical finite element model. Proceedings of the 4th CACRCS DAYS 2023; Sep 13–15; Parma, Italy; 2023. p. 159–163.
42. Vereecken E, Botte W, Caspeele R, Lombaert G. Updating of the corrosion degree based on visual data combined with strain or modal data. Presented at IABSE Congress: Structural Engineering for Future Societal Needs, vol. 21; 2021 September 22–24; Ghent, Belgium. Ghent: IABSE Congress; 2021. p. 1092–1101.
43. Belletti B, Scolari M, Vecchi F. PARC_CL 2.0 crack model for NLFEA of reinforced concrete structures under cyclic loadings. Comput Struct. 2017;191:165–79.
44. Franceschini L, Vecchi F, Belletti B. The PARC_CL 2.1 crack model for NLFEA of reinforced concrete elements subjected to corrosion deterioration. Corros Mater Degrad. 2021;2(3):474–92.
45. Belletti B, Vecchi F. A crack model for corroded reinforced concrete elements subject to cyclic loading. Proc Inst Civ Eng Bridge Eng. 2022;175(1):50–65.
46. Belletti B, Vecchi F, Bandini C, Andrade C, Montero JS. Numerical evaluation of the corrosion effects in prestressed concrete beams without shear reinforcement. Struct Concr. 2020;21(5):1794–809.
47. Michelini E, Belletti B, Franceschini L, Martinelli E. Time-dependent seismic fragility curves for existing RC core-wall buildings exposed to corrosion. Struct Concr. 2022;24:1–19.
48. Flores Ferreira K, Rampini MC, Zani G, Colombo M, di Prisco M. Experimental investigation on the use of fabric-reinforced cementitious mortars for the retrofitting of reinforced concrete dapped-end beams. Struct Concr. 2023;24:1–29.
49. Di Carlo F, Meda A, Molaioni F, Rinaldi Z. Experimental evaluation of the corrosion influence on the structural response of Gerber half-joints. Eng Struct. 2023;285, January:116052.
50. Molaioni F, Rinaldi Z. Effects of steel ties layout and corrosion on structural behavior of Gerber half-joints. 14th fib International PhD Symposium in Civil Engineering; 2022. p 17–24.
51. Fib Model Code 2010, fib Model Code for Concrete Structures 2010. Ernst & Sohn, Lausanne, Switzerland; 2013.
52. Hendriks MAN, de Boer A, Belletti B. Guidelines for nonlinear finite element analysis of concrete structures, Report RTD, 1016-1. Utrecht, Netherlands: Rijkswaterstaat Centre for Infrastructure; 2017.
53. Belletti B, Damoni C, Hendriks MAN. Development of guidelines for nonlinear finite element analyses of existing reinforced and pre-stressed beams. Eur J Environ Civ Eng. 2011;15(9):1361–84.
54. Simulia. ABAQUS standard user's manual, version 2021. United States: Dassault Systemes Simulia Corp.; 2021.
55. Vecchi F, Belletti B. Capacity assessment of existing RC columns. Buildings. 2021;11(4):161.
56. Desnerck P, Lees JM, Morley CT. The effect of local reinforcing bar reductions and anchorage zone cracking on the load capacity of RC half-joints. Eng Struct. 2017;152:865–77.
57. Quadri AI, Fujiyama C. Response of reinforced concrete dapped-end beams exhibiting bond deterioration subjected to static and cyclic loading. J Adv Concr Technol. 2021;19(5):536–54.
58. Mak MWT, Sheasby MP, Lees JM. Effects of anchorage deterioration on the shear behaviour of reinforced concrete half-joint

17517648, 2024, 2, Downloaded from https://onlinelibrary.wiley.com/doi/10.1002/suco.202301020 by University Degli Studi Di Parma Settore Biblioteche, Wiley Online Library on [15/05/2024]. See the Terms and Conditions (https://onlinelibrary.wiley.com/terms-and-conditions) on Wiley Online Library for rules of use; OA articles are governed by the applicable Creative Commons License

beams. Proceedings of the fib Symposium 2020 on Concrete Structures for Resilient Society; 2020 Nov 22–24; Shanghai, China; 2020. p 1786–1792.
59. Tuutti K. Corrosion of steel in concrete. Stockholm, Sweden: Swedish Cement and Concrete Research Institute; 1982.
60. CONTECVET IN30902I, 2001. A validated user's manual for assessing the residual life of concrete structures, DG Enter-prise, CEC. Available from: www.ietcc.csic.es or www.geocisa.es
61. EN-206-1:2013+A2:2021, "Concrete-specification, performance, production and confirmity," 2021.
62. Val DV. Deterioration of strength of RC beams due to corrosion and its influence on beam reliability. J Struct Eng. 2007;133(9): 1297–306.
63. Coronelli D, Gambarova P. Structural assessment of corroded reinforced concrete beams: modeling guidelines. J Struct Eng. 2004;130(8):1214–24.
64. Castel A, Khan I, François R, Gilbert RI. Modeling steel concrete bond strength reduction due to corrosion. ACI Struct J. 2016;113(5):973–82.
65. François R, Castel A, Vidal T. A finite macro-element for corroded reinforced concrete. Mater Struct. 2007;39(5): 571–84.
66. Calcavecchia B, Ravasini S, Belletti B, Rinaldi Z, Di Carlo F, Molaioni F. Numerical approach to evaluate the load bearing capacity of RC dapped-end beams subjected to corrosion. Proceedings of the 4th CACRCS DAYS 2023; Sep–15; Parma, Italy; 2023. p. 253–256.

AUTHOR BIOGRAPHIES

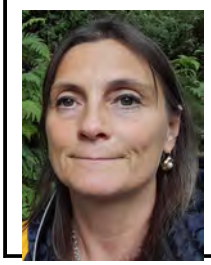

Beatrice Belletti, Full Professor in Structural Engineering at Department of Engineering and Architecture, University of Parma, Parco Area delle Scienze 181/A, 43124 Parma, Italy. Email: beatrice.belletti@unipr.it

Biagio Calcavecchia, PhD student at Department of Engineering and Architecture, University of Parma, Parco Area delle Scienze 181/A, 43124 Parma, Italy. Email: biagio.calcavecchia@unipr.it

Daniele Ferretti, Associate Professor in Structural Engineering at Department of Engineering and Architecture, University of Parma, Parco Area delle Scienze 181/A, 43124 Parma, Italy. Email: daniele.ferretti@unipr.it

Simone Ravasini, Research fellow at Department of Engineering and Architecture, University of Parma, Parco Area delle Scienze 181/A, 43124 Parma, Italy. Email: simone.ravasini@unipr.it

How to cite this article: Belletti B, Calcavecchia B, Ferretti D, Ravasini S. Capacity assessment of uncorroded and corroded dapped-end beams by NLFE and strut-and-tie based methods. Structural Concrete. 2024;25(2): 1275–304. https://doi.org/10.1002/suco.202301020

17517648, 2024, 2, Downloaded from https://onlinelibrary.wiley.com/doi/10.1002/suco.202301020 by University Degli Studi Di Parma Settore Biblioteche, Wiley Online Library on [15/05/2024]. See the Terms and Conditions (https://onlinelibrary.wiley.com/terms-and-conditions) on Wiley Online Library for rules of use; OA articles are governed by the applicable Creative Commons License